

High-temperature superconductivity in monolayer $\text{Bi}_2\text{Sr}_2\text{CaCu}_2\text{O}_{8+\delta}$

<https://doi.org/10.1038/s41586-019-1718-x>

Received: 2 April 2019

Accepted: 23 August 2019

Published online: 30 October 2019

Yijun Yu^{1,2,3,7}, Ligu Ma^{1,2,3,7*}, Peng Cai^{1,2,3,7}, Ruidan Zhong⁴, Cun Ye^{1,2,3}, Jian Shen^{1,2,3}, G. D. Gu⁴, Xian Hui Chen^{3,5,6*} & Yuanbo Zhang^{1,2,3*}

Although copper oxide high-temperature superconductors constitute a complex and diverse material family, they all share a layered lattice structure. This curious fact prompts the question of whether high-temperature superconductivity can exist in an isolated monolayer of copper oxide, and if so, whether the two-dimensional superconductivity and various related phenomena differ from those of their three-dimensional counterparts. The answers may provide insights into the role of dimensionality in high-temperature superconductivity. Here we develop a fabrication process that obtains intrinsic monolayer crystals of the high-temperature superconductor $\text{Bi}_2\text{Sr}_2\text{CaCu}_2\text{O}_{8+\delta}$ (Bi-2212; here, a monolayer refers to a half unit cell that contains two CuO_2 planes). The highest superconducting transition temperature of the monolayer is as high as that of optimally doped bulk. The lack of dimensionality effect on the transition temperature defies expectations from the Mermin–Wagner theorem, in contrast to the much-reduced transition temperature in conventional two-dimensional superconductors such as NbSe_2 . The properties of monolayer Bi-2212 become extremely tunable; our survey of superconductivity, the pseudogap, charge order and the Mott state at various doping concentrations reveals that the phases are indistinguishable from those in the bulk. Monolayer Bi-2212 therefore displays all the fundamental physics of high-temperature superconductivity. Our results establish monolayer copper oxides as a platform for studying high-temperature superconductivity and other strongly correlated phenomena in two dimensions.

In systems with reduced dimensions, long-range order (superconductivity in particular) is strongly suppressed^{1,2}, as in the case of conventional Bardeen–Cooper–Schrieffer-type superconductors^{3,4}, and yet all high-temperature copper oxide superconductors have a layered structure with varying degrees of anisotropy. This apparent dichotomy may be the key to high-temperature superconductivity (HTS)^{5–9}, and it raises the question of whether HTS and various correlated phenomena associated with it are different in two dimensions. This question is important for two reasons. First, most HTS theories are based on purely two-dimensional (2D) models^{10–12}, whereas experiments show that supercurrent phase coherence¹³, charge ordering^{14,15} and charge dynamics¹⁶ all have a 3D nature¹⁷. Second, much of what we know about HTS came from experimental tools such as scanning tunnelling microscopy/spectroscopy (STM/STS) and angle-resolved photoemission spectroscopy (ARPES) that probe the surface of the materials^{18–36}; HTS as a bulk property was inferred from the surface measurements. The bulk–surface correspondence becomes ideal if the HTS is truly 2D. To resolve these issues experimentally, an isolated monolayer high-temperature superconductor is needed. Such an atomically thin crystal

would represent an ideal correlated 2D system for exploring quantum phenomena in reduced dimensions.

Monolayer HTS has previously been studied mostly in epitaxial oxide heterostructures^{37–39}, where the active layers are buried between interfaces. Such systems are not accessible to spectroscopic tools such as STM/STS and ARPES. In recent years, an alternative, top-down approach has emerged: it has become possible to mechanically exfoliate monolayer atomic crystals (termed ‘2D materials’) from the layered bulk^{40,41}. High-quality 2D materials ranging from insulators to metals and superconductors⁴² have been produced this way.

Experimentally extracting monolayers from bulk high-temperature superconductors, however, turned out to be extremely challenging. Although many of the bulk high-temperature superconductors are considered stable under ambient conditions, they are highly prone to chemical degradation when thinned to monolayers. Indeed, monolayer Bi-2212 has been found to be insulating^{41,43} or superconducting with a much reduced transition temperature (T_c)⁴⁴. The suppression is seemingly consistent with increased fluctuations expected in 2D superconductors. But given that the material is extremely sensitive

¹State Key Laboratory of Surface Physics and Department of Physics, Fudan University, Shanghai, China. ²Institute for Nanoelectronic Devices and Quantum Computing, Fudan University, Shanghai, China. ³Collaborative Innovation Center of Advanced Microstructures, Nanjing, China. ⁴Condensed Matter Physics and Materials Science Department, Brookhaven National Laboratory, Upton, NY, USA. ⁵Hefei National Laboratory for Physical Science at Microscale and Department of Physics, University of Science and Technology of China, Hefei, China. ⁶Key Laboratory of Strongly Coupled Quantum Matter Physics, University of Science and Technology of China, Hefei, China. ⁷These authors contributed equally: Yijun Yu, Ligu Ma, Peng Cai.

*e-mail: malg.phys@gmail.com; chenxh@ustc.edu.cn; zhyb@fudan.edu.cn

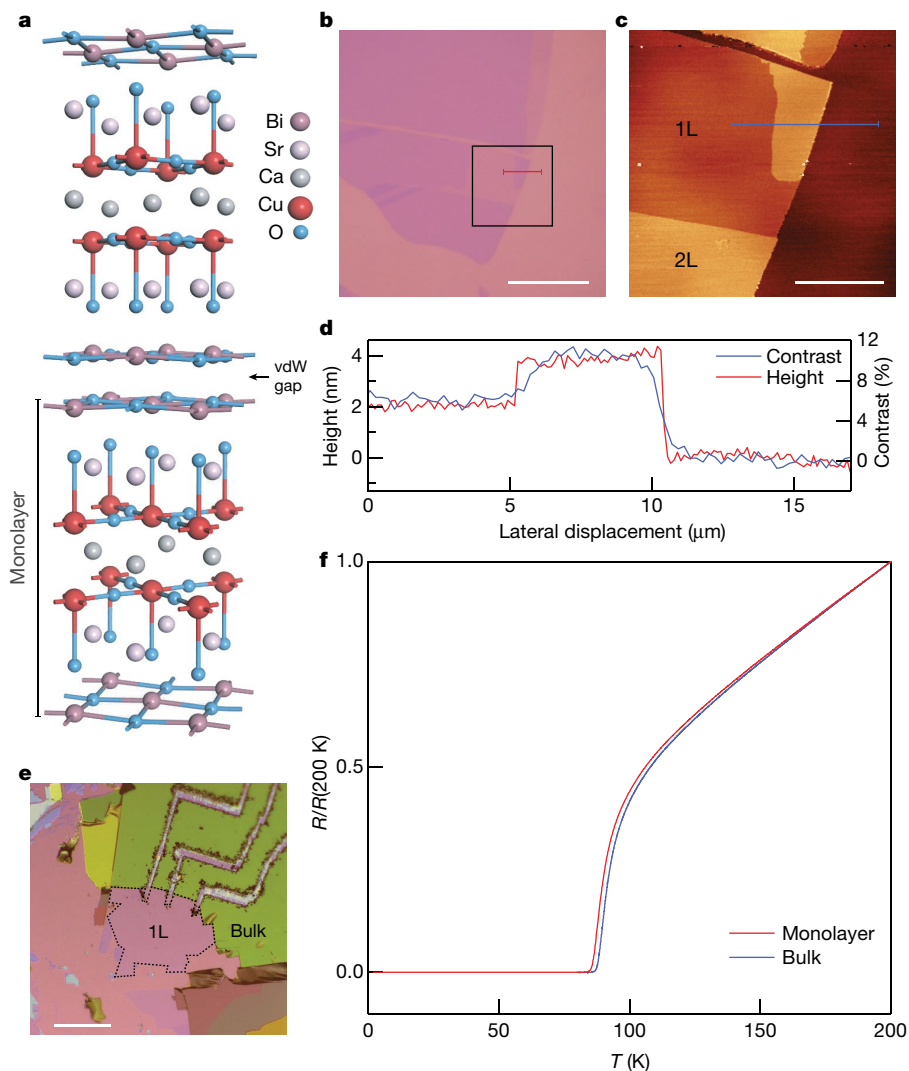


Fig. 1 | Fabrication and characterization of atomically thin Bi-2212 transport devices. **a**, Atomic structure of Bi-2212. ‘Monolayer’ refers to a half unit cell in the out-of-plane direction that contains two CuO_2 planes. The monolayers are separated by van der Waals gaps in bulk Bi-2212. **b**, Optical image of a typical Bi-2212 thin flake exfoliated on Si wafer covered with 285-nm-thick SiO_2 . Scale bar, 30 μm . **c**, Atomic force microscopy (AFM) image of the same flake shown in **b** (region marked by the black square). L, layer. Scale bar, 10 μm . **d**, Cross-sectional profile of optical contrast along the red line in **b**, in comparison with the cross-

sectional profile of AFM topography at the same location (blue line in **c**). The quantized steps in contrast and height profiles correspond to monolayer terraces of Bi-2212. **e**, Optical image of a monolayer Bi-2212 device. The bulk flake in contact with the monolayer is cut into separate pieces, which serve as electrical leads for transport measurements. Scale bar, 100 μm . **f**, Typical temperature-dependent resistance of a monolayer Bi-2212 sample (red) in comparison with that of an optimally doped bulk crystal (blue). Resistances are normalized by their values at $T = 200$ K.

to environment and to doping variations, all extrinsic factors must be eliminated before ascribing the reduction of T_c in monolayers to the effect of dimensionality. The outstanding challenge has been to fabricate high-quality monolayer crystals and probe their intrinsic electronic structure.

Here we overcome these challenges by developing sample fabrication processes that preserve the intrinsic properties of monolayer Bi-2212. We first pinpoint two main causes of sample degradation—reaction with water vapour and rapid loss of oxygen dopant. We find that the degradation slows down in a cold, inert environment, in which pristine monolayer Bi-2212 can be obtained. Unlike the bulk crystal, the monolayer Bi-2212 is extremely tunable: we can continuously vary its doping level in situ and map out major phases from the over-doped regime to the Mott insulating regime, in a single monolayer device. We find that the highest T_c of the monolayer is as high as that of optimally doped bulk. Moreover, STM/STS study reveals that the monolayer develops the same rich set of phases—HTS, pseudogap, charge order and Mott

insulating phase, in particular—that were observed on the bulk surface. Detailed characterization of the phases reveals that they are indistinguishable from those in the bulk. A monolayer, therefore, contains all the essential physics of Bi-2212: that is, HTS in Bi-2212 is essentially a 2D phenomenon.

Fabricating pristine monolayer Bi-2212

We start with bulk Bi-2212 with a slightly modified stoichiometry, $\text{Bi}_{1.9}\text{Sr}_{2.1}\text{CaCu}_2\text{O}_{8+\delta}$, which has a highest T_c of 88 K at optimal doping. In a monolayer Bi-2212, two CuO_2 planes—separated by a Ca layer—are sandwiched between SrO and BiO planes to form a charge-neutral, septuple-layered slab as shown in Fig. 1a. The parent compound of Bi-2212 is an antiferromagnetic Mott insulator⁴⁵. Doping holes into the CuO_2 planes generates a pseudogap phase that is characterized by strong depletion of density of states (DOS) near the Fermi level^{18–20}. As the doping level p (holes per CuO_2 plaquette) increases, the pseudogap phase evolves

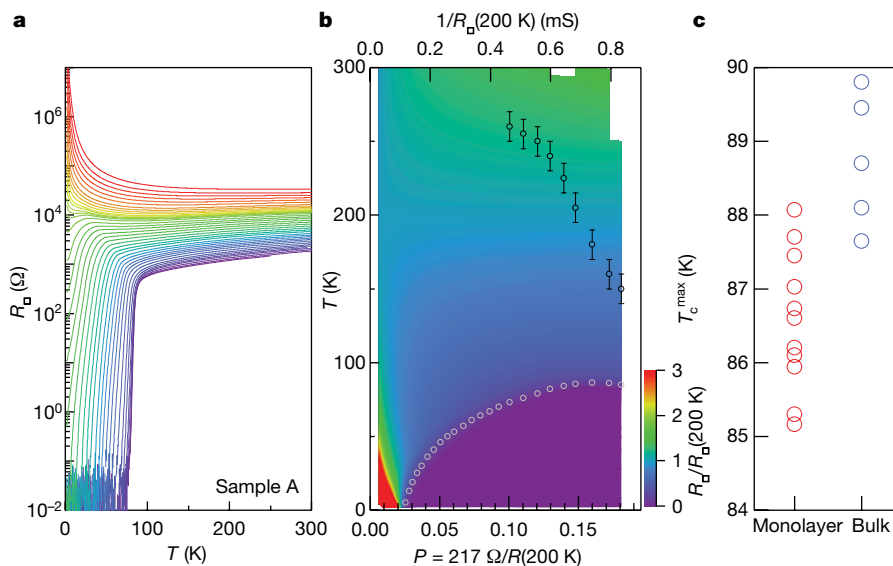


Fig. 2 | Tunable high-temperature superconductivity in monolayer Bi-2212.

a, Temperature-dependent resistivity $R_{\square}(\rho, T)$ of a monolayer Bi-2212 (sample A) that is initially over-doped. Data were acquired between annealing cycles that progressively lower the doping level of the sample (from purple to red). **b**, Conductivity plotted as a function of temperature and doping level. Doping level p is determined from $p = 217 \Omega/R_{\square}(T = 200 \text{ K})$. Black circles denote the onset of the pseudogap state at T^* . Here the vertical error bars represent uncertainties in locating T^* at which the temperature-dependent resistance

deviates from linear behaviour. White circles mark the superconducting transition temperature T_c . The phase diagram spans the optimal doping at which T_c reaches its maximum value T_c^{max} . **c**, T_c^{max} obtained from different monolayer Bi-2212 samples (an example is shown in **b**), in comparison with T_c in optimally doped bulk crystals. The highest T_c^{max} represents the maximum T_c of the most intrinsic monolayer in our experiment, and its value lies within the uncertainty range of the T_c in optimally doped bulk.

into a superconducting phase with highest T_c reaching 91 K at an optimal doping level of $p = 0.16$ (ref. ⁴⁶). Oxygen doping is therefore a key variable that determines the electronic structure in Bi-2212. Because the van der Waals interaction between the layers is weak, atomically thin Bi-2212 flakes can be obtained through mechanical exfoliation on an oxygen-plasma-treated SiO_2 surface⁴⁷. Figure 1b and c displays optical images of few-layer Bi-2212 in which the monolayer region is as large as several hundreds of micrometres in diameter (the number of layers is identified from the optical contrast, which correlates well with the thickness of the crystals determined from atomic force microscopy; Fig. 1d).

The exfoliated monolayer Bi-2212 is extremely sensitive to its environment. We find that the monolayers are insulating if the specimen is prepared under ambient conditions, consistent with previous reports^{41,43}. A systematic investigation (see Extended Data Table 1 and Extended Data Fig. 1) reveals that exposing the monolayers to air, albeit briefly, renders them insulating. Guided by the investigation, we succeeded in obtaining high-quality, intrinsic monolayer Bi-2212 by fabricating samples on a cold stage kept at $-40 \text{ }^\circ\text{C}$ inside an Ar-filled glove box with water and oxygen content below 0.1 ppm. Finally, we make electrical contacts to the monolayer flakes by cold-welding indium/gold microelectrodes (see Methods and Extended Data Table 1) on top. The flakes are then cut into an appropriate geometry with a sharp tip (Fig. 1e), and quickly transferred into an evacuated sample chamber for subsequent transport measurements. We have also obtained monolayer Bi-2212 of similar quality at low temperatures under ultra-high vacuum (UHV) for separate STM/STS study; details of the sample fabrication procedure are provided in the Methods.

Figure 1f shows the normalized resistance of a monolayer in comparison with that of optimally doped bulk Bi-2212. The monolayer retains HTS, and the sharp superconductivity transition signifies the high quality of the sample. More surprisingly, the T_c of the monolayer is almost as high as the optimal T_c in the bulk, indicating that HTS in 2D monolayer Bi-2212 does not differ appreciably from that in 3D bulk. This is corroborated by an accurate quantitative comparison of monolayer and bulk T_c , which we discuss below.

Tunable high-temperature superconductivity

The reduction in dimensionality produces a key advantage: the HTS in monolayer Bi-2212 becomes extremely tunable. The tunability stems from the fact that both sides of the monolayer are exposed, making it easy for interstitial oxygen to escape from or enter the crystal. Specifically, we find that mild vacuum annealing at temperatures between 300 K and 380 K drives oxygen out of the monolayer. Meanwhile, annealing at about 200 K in ozone (partial pressure approximately 0.5 mbar) increases the oxygen concentration (Extended Data Fig. 2). These findings enable us to continuously vary the doping level and track the evolution of various phases, including superconductivity, from an over-doped to deeply under-doped regime (and vice versa) in a single monolayer sample. Figure 2a displays a set of measurements of temperature-dependent resistivity, $R_{\square}(T)$, of a monolayer Bi-2212 (sample A), acquired between annealing treatments at 300–380 K in vacuum (base pressure $<10^{-4}$ mbar). The annealing treatments progressively lower the hole doping level in the monolayer and induce a transition from superconducting to insulating behaviour. Meanwhile, the room-temperature resistivity increases by one order of magnitude from about 1 k Ω to about 30 k Ω . Details of the transition become more apparent when the resistivity of the same sample (normalized to its value at $T = 200 \text{ K}$) is plotted as a function of temperature and hole doping level p , as shown in Fig. 2b. (Here the hole doping level is determined from $p = \text{const.}/R_{\square}(T = 200 \text{ K})$; the value of the constant (const.) is chosen so that $p = 0.16$ at optimal doping^{48,49}, and the precise value of p does not affect our conclusions.) As p decreases, T_c (defined as the temperature at which $d^2R_{\square}/dT^2 = 0$; see Extended Data Fig. 3) rises at first, then falls continuously, giving rise to a superconducting dome that ends at $p \approx 0.022$. An insulating phase appears next to the superconducting dome. In addition, we observe at $T^* > T_c$ the onset of the pseudogap phase that is marked by deviation from a linear $R_{\square}(T)$ in the normal state of a high-temperature superconductor under various doping levels (open black circles in Fig. 2b; see Extended Data Fig. 3 for detailed analysis). Figure 2b, therefore, maps out a phase

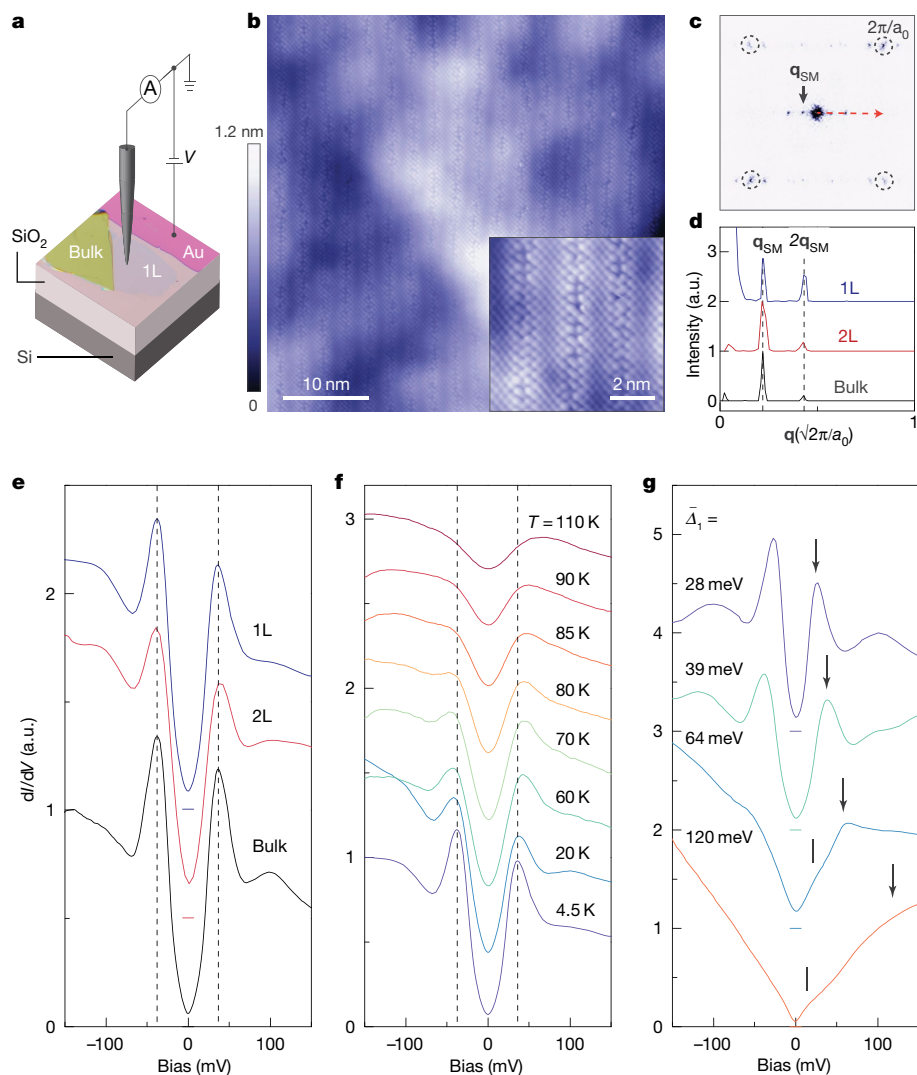


Fig. 3 | Tunnelling spectroscopy of monolayer Bi-2212. **a**, Schematic illustration of the STM measurement set-up. Monolayer Bi-2212 (and the bulk crystal nearby) is electrically connected to a pre-patterned Au electrode, which provides a returning path for the tunnelling current. **b**, High-resolution STM topograph of a monolayer Bi-2212. The image was taken at a junction resistance of $2\text{ G}\Omega$ and a sample bias voltage of -300 mV . Inset: magnified view of top Bi atoms and supermodulation ridges. **c**, Fourier transform of the STM topograph in **b**. Peaks are clearly visible at multiples of supermodulation wavevector \mathbf{q}_{SM} . Bragg peaks of the atomic lattice are marked by broken circles. **d**, Line cut of the Fourier transform in **c** along the $[1,1]$ direction. Monolayer curve (1L, blue) is compared with bilayer (2L, red) and bulk (black) data; peaks at \mathbf{q}_{SM} and $2\mathbf{q}_{\text{SM}}$ align within an uncertainty of 1.5% of $2\pi/a_0$.

e, Spatially averaged differential conductance spectra acquired on monolayer, bilayer and bulk Bi-2212 at near optimal doping. Broken lines mark the position of coherence peaks. The horizontal bars mark the zero of each curve. **f**, Spatially averaged spectral temperature dependence on a nearly optimal doped monolayer Bi-2212 showing a smooth transition from the superconducting to pseudogap state at $T \approx 85\text{ K}$. **g**, Evolution of spatially averaged tunnelling spectra of monolayer Bi-2212 with diminishing doping level p . Here the doping level is characterized by $\Delta_1(p)$. The energies Δ_1 (black arrows) are extracted at the pseudogap edge, and the energies Δ_0 (vertical bars) are identified as the 'kink' energy²³. Curves are offset for clarity, and horizontal bars mark the zero of each curve.

diagram of the monolayer that is strikingly similar to that of bulk copper oxides⁵⁰.

Close examination of the phase diagram in Fig. 2b provides further insights into the 2D HTS in monolayer Bi-2212. We focus on the high T_c that characterizes the superconducting transition in the monolayer. Specifically, we use the phase diagram to accurately determine how much, if at all, T_c is suppressed in the monolayer compared with in the bulk. Because T_c strongly depends on hole doping level, a comparison is valid only when it is made at the same doping level. The maximum T_c at optimal doping, T_c^{max} , therefore serves as a natural metric for such comparison, given that varying the sample thickness does not alter the optimal doping level itself. Figure 2c summarizes the measured T_c^{max} of monolayer Bi-2212 in comparison with the T_c of optimally doped bulk

crystals. (Here T_c^{max} of monolayers was extracted from phase diagrams, exemplified in Fig. 2b, and we ensured that the superconducting domes of all monolayer samples spanned the optimal doping so that T_c^{max} could be reliably determined; T_c^{max} determined by different methods is shown in Extended Data Fig. 3.) Both datasets exhibit appreciable spread that most likely reflects variations in the impurity level in different specimens. More importantly, the highest T_c^{max} of 88.1 K that represents the most intrinsic monolayer is within the uncertainty of optimal bulk T_c . The difference of about 2% between the average of T_c^{max} in the monolayer and the average of optimal T_c in bulk may be explained by inevitable slight sample degradation from our fabrication process. Our observations therefore reveal a robust 2D HTS in monolayer Bi-2212 with optimal transition temperature as high as that in 3D bulk.

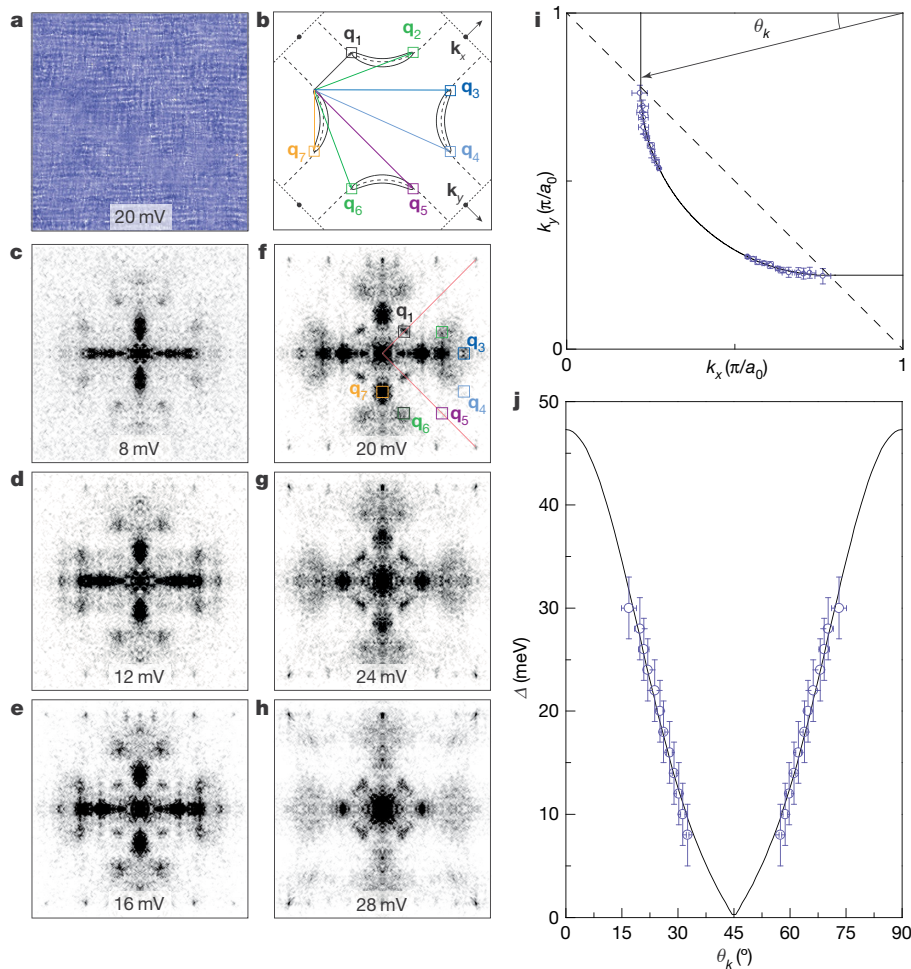


Fig. 4 | Quasi-particle interference and superconducting gap in monolayer Bi-2212. **a**, Representative conductance ratio map $Z(\mathbf{r}, E)$ obtained at $E = 20$ mV on the same area as in Fig. 3b. **b**, Illustration of the octet model for Bogoliubov quasiparticle interference in Bi-2212 at a given energy. The octet ends of four banana-shaped constant-energy contours have maximum density of states. Quasi-particle scattering between these eight regions produces seven primary scattering \mathbf{q} -vectors, \mathbf{q}_1 to \mathbf{q}_7 , labelled by coloured squares. **c–h**, Fourier transform of the conductance ratio map $|Z(\mathbf{q}, E)|$. The Fourier transforms are mirror-symmetrized and normalized to their average value. E is labelled on each panel. In particular, **f** displays the Fourier transform of the conductance ratio map in **a**. Red solid lines indicate the atomic Bragg vectors at $(2\pi/a_0, 0)$ and $(0, 2\pi/a_0)$. Of the total of seven independent scattering vectors (coloured

squares) prescribed by the octet model illustrated in **b**, five are observed as peaks in the Fourier transform; \mathbf{q}_4 and \mathbf{q}_5 are too weak to be detected. **i**, Loci of the ends of banana-shaped constant-energy contours extracted from dispersion of the \mathbf{q} -vectors. Locations of the loci represent the underlying Fermi surface. Solid line is a fit to the data with a circular arc joined with two straight lines. Broken line marks the antiferromagnetic zone boundary. **j**, Superconducting gap Δ_{SC} as a function of Fermi surface angle θ_k . Δ_{SC} is extracted from the measured position of scattering vectors \mathbf{q}_1 to \mathbf{q}_7 (excluding \mathbf{q}_4 and \mathbf{q}_5) following the procedure described in refs.^{24,26}. Solid line is a fit to the data with d -wave gap function $\Delta(\theta_k) = \Delta_{QPI}[A \cos(2\theta_k) + (1 - A)\cos(6\theta_k)]$, where $\Delta_{QPI} = 47.3$ meV and $A = 0.844$ are fitting parameters.

Monolayer topography and tunnelling spectroscopy

STM topography measurement (schematic set-up shown in Fig. 3a) confirms the high quality of monolayer Bi-2212, which retains the original atomic structure found in the bulk crystals. Figure 3b displays the atom-resolved topography of the top BiO plane of a Bi-2212 monolayer. The surfaces are as clean as the bulk surface and are continuous over macroscopic distances (about 100 μm ; Extended Data Fig. 6). Nearly commensurate supermodulation ridges along the $[\bar{1}10]$ direction—a distinctive feature in Bi-based bulk copper oxides¹⁸—are clearly observed. Fourier transform of the topography images reveals that the period of the supermodulation \mathbf{q}_{SM} exactly matches that on the bulk surface (Fig. 3c, d); no additional surface reconstructions were detected. Despite the identical atomic structure, monolayer Bi-2212 does exhibit a feature not seen on the bulk surface: large scale corrugations with a root-mean-square (r.m.s.) value of 0.2 nm, in contrast to the flat surface of the bulk crystal. We attribute the corrugations to the underlying substrate: few-layer Bi-2212 may become flexible and

partially conform to the rough surface of amorphous SiO_2 (r.m.s. approximately 0.25 nm).

We now turn to the electronic structure of monolayer Bi-2212. We note that a variety of spectroscopy studies revealed a rich set of phases that are characterized by two energy scales, referred to as Δ_0 and Δ_1 , in bulk Bi-2212 (refs.^{20,21}). Specifically, excitations in the superconducting state occur at energies $E \lesssim \Delta_0$, whereas charge-order and other highly correlated broken-symmetry states appear at pseudogap energy scale $E \approx \Delta_1$; the competition or cooperation between these intertwined phases remains one of the central problems of HTS (refs.^{5,12}). In the following, we examine these strongly correlated states in monolayer Bi-2212.

Figure 3e displays the differential conductance spectra $g(E)$, which is proportional to the DOS at energy E , of monolayer and bilayer samples cleaved from a nearly optimally doped bulk crystal with $T_c = 88$ K (referred to as OP88). Here the spectra are spatial averages of the local differential conductance spectra $g(\mathbf{r}, E = eV) \equiv dI/dV|_{\mathbf{r}, V}$ over a 500 \AA

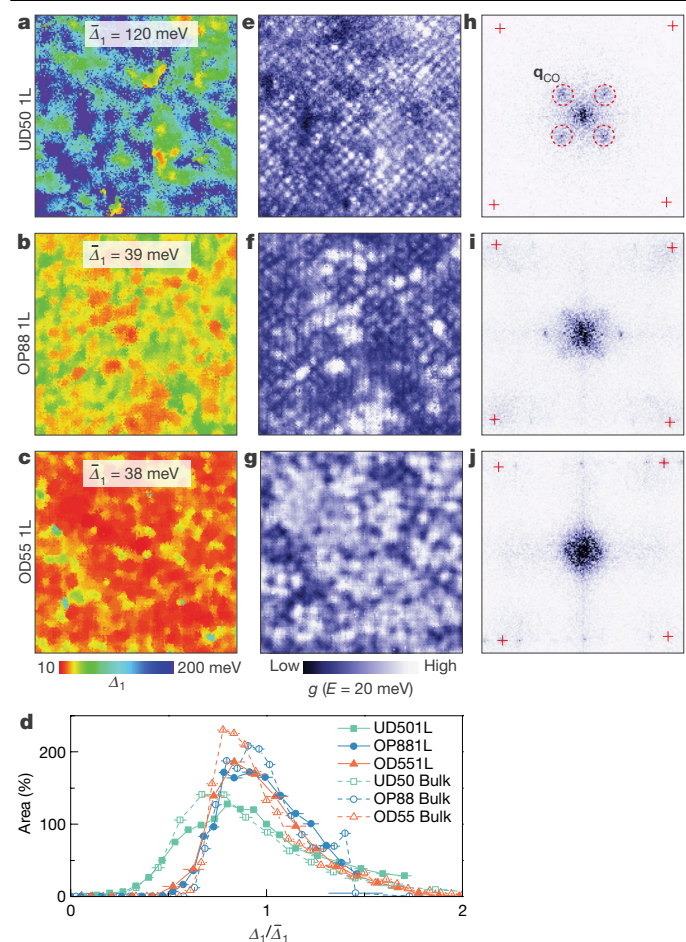


Fig. 5 | Electronic inhomogeneity and charge-ordered state in monolayer Bi-2212. **a–c**, Gap maps $\Delta_1(\mathbf{r})$ obtained on monolayer Bi-2212. The monolayers are obtained from bulk crystals UD50 (under-doped, $T_c = 50$ K), OP88 (optimally doped, $T_c = 88$ K) and OD55 (over-doped, $T_c = 55$ K). Field of view, $400 \text{ \AA} \times 400 \text{ \AA}$. $\bar{\Delta}_1$ denotes the average value of Δ_1 over the entire field of view. $\Delta_1(\mathbf{r})$ in **a** was determined from fitting each local tunnelling spectrum using the method described in ref. ³⁶. Values of $\Delta_1(\mathbf{r})$ in **b** and **c** were extracted as the energy separation between two coherence peaks in each local tunnelling spectrum. **d**, Histograms of $\Delta_1(\mathbf{r})$ shown in **a–c** normalized by their mean value. The normalized gap distributions in monolayers are highly similar to those of bulk source crystals (Extended Data Fig. 9). **e–g**, Conductance maps $g(\mathbf{r}, E) = dI/dV(\mathbf{r}, E)$ recorded at $E = 20$ meV on the same areas shown in **a–c**. **h–j**, Fourier transforms of $g(\mathbf{r}, E = 20$ meV) in **e–g**. Charge-order peaks are clearly resolved at $\mathbf{q} = (\pm 0.25, 0)2\pi/a_0$ and $(0, \pm 0.25)2\pi/a_0$ (marked by broken circles) in under-doped monolayer. Red crosses mark lattice wavevectors at $(\pm 2\pi/a_0, 0)$ and $(0, \pm 2\pi/a_0)$.

$\times 500 \text{ \AA}$ field of view; I and V are tunnelling current and sample-bias voltage, respectively, and e is the charge of an electron. The V-shaped superconducting energy gap and the large coherence peaks on both sides of the gap are clearly observed in the spectra. The size of the gap, defined as half the separation between two coherence peaks, Δ_0 , in the monolayer and bilayer is almost identical to that in the bulk (Fig. 3e, black curve) from which the monolayer and bilayer were obtained. Close examination reveals that the monolayer and bilayer spectra also faithfully reproduce the fine details, the dip–hump structure outside of the gap and the electron–hole asymmetric background in particular, that are found in the bulk spectrum¹⁸. Differential conductance spectra at elevated temperatures show that the pseudogap state, too, persists in monolayer Bi-2212. The pseudogap state manifests as a gap in $g(E)$ well above the T_c of the bulk source crystal (Fig. 3f). Finally, we note that Δ_1 coincides with Δ_0 in the nearly optimally doped monolayer. On lower-

ing the doping level, however, the two energy scales diverge: Δ_1 moves to higher energies, whereas Δ_0 becomes smaller (Fig. 3g), consistent with the behaviour in bulk copper oxide superconductors^{18,23}. The close match between the monolayer and bulk spectra is the first indication that the superconducting state (and electronic structures associated with it) remains intact in the 2D limit.

Quasi-particle interference and superconducting gap

The low-energy excitations inside the superconducting energy gap carry crucial information on the superconducting state. The excitations, also known as Bogoliubov quasiparticles, scatter off impurities and produce interference patterns that can be detected by spatial mapping of the tunnelling conductance in $g(\mathbf{r}, eV)$ at a given bias V on the bulk Bi-2212 surface^{21,24}. Further, the Fourier transform of the interference patterns reveals maxima at a set of energy-dependent wavevectors \mathbf{q}_i ($i = 1, \dots, 7$)—a result of elastic scattering between the eight high-joint-density-of-state loci of the ‘banana-shaped’ constant energy contour of Bogoliubov quasiparticles²⁴ (referred to as the ‘octet model’; Fig. 4b). The quasi-particle interference has therefore been a powerful tool for reconstructing the superconducting gap dispersion $\Delta(\mathbf{k})$ of copper oxide superconductors^{18,26}.

We used the quasi-particle interference technique to probe $\Delta(\mathbf{k})$ in monolayer Bi-2212. We focus on the conductance ratio map $Z(\mathbf{r}, E = eV) \equiv g(\mathbf{r}, +eV)/g(\mathbf{r}, -eV)$, which eliminates systematic errors related to the tunnelling setpoint associated with directly mapping the conductance $g(\mathbf{r}, eV)$ (ref. ²⁶). Figure 4a displays an example of the conductance ratio map of monolayer Bi-2212 obtained at $E = 20$ meV. The Fourier transform of the conductance ratio map, $|Z(\mathbf{q}, E = eV)|$ shows clear maxima at \mathbf{q}_i that are fully consistent with the octet model, except that peaks at \mathbf{q}_4 and \mathbf{q}_5 are too weak to be detected (Fig. 4f). As the tunnelling bias V is varied, we observe that the measured \mathbf{q}_i disperse with energy $E = eV$, and the dispersions $\mathbf{q}_i(E)$ are again consistent with those expected from the octet model (Extended Data Figs. 7 and 8). The dispersions $\mathbf{q}_i(E)$ allow us to extract the energy-dependent locations of the octet ends of the ‘bananas’ in \mathbf{k} space, and the obtained loci can be interpreted as the normal-state Fermi surface²⁴. Our result, shown in Fig. 4i, is consistent with a cylindrical Fermi surface centred at (π, π) that is observed in bulk Bi-2212 and various other bulk copper oxide superconductors²⁶. Finally, we determine the superconducting gap dispersion $\Delta(\mathbf{k})$ from $\mathbf{q}_i(E)$. Figure 4j displays the measured superconducting gap energy of the monolayer as a function of θ_k along the Fermi surface. The data agree with the d -wave superconducting gap dispersion of bulk Bi-2212 at similar doping level²³. We therefore conclude that reducing the material’s dimensions from three to two does not fundamentally alter the superconducting gap structure.

Electronic inhomogeneity and charge-ordered state

Next, we focus on the electronic structure of monolayer Bi-2212 beyond the superconducting energy gap Δ_0 . In particular, the energy scale Δ_1 is associated with the anti-nodal pseudogap and other correlated states that are intricately linked to superconductivity²¹. In contrast to the relatively homogeneous superconducting gap Δ_0 , the pseudogap Δ_1 varies widely at the nanometre length scale on bulk copper oxides¹⁸. To study the inhomogeneity in monolayer Bi-2212, we extract Δ_1 from the local differential conductance spectra collected on a dense array of locations on samples at various doping levels, and construct the gap map $\Delta_1(\mathbf{r})$ as shown in Fig. 5a–c. Similar to previous measurements on bulk Bi-2212, we find that wide, nanometre-scale variations in Δ_1 diminish as the doping level increases in the monolayer; meanwhile Δ_1 averaged over the entire field of view, $\bar{\Delta}_1$, shifts to lower energies. Close examination of Δ_1 histograms reveals that $\bar{\Delta}_1$ in monolayers is in general larger than that in bulk source crystals from which the monolayers are cleaved (Extended Data Fig. 9), and the deviation varies from

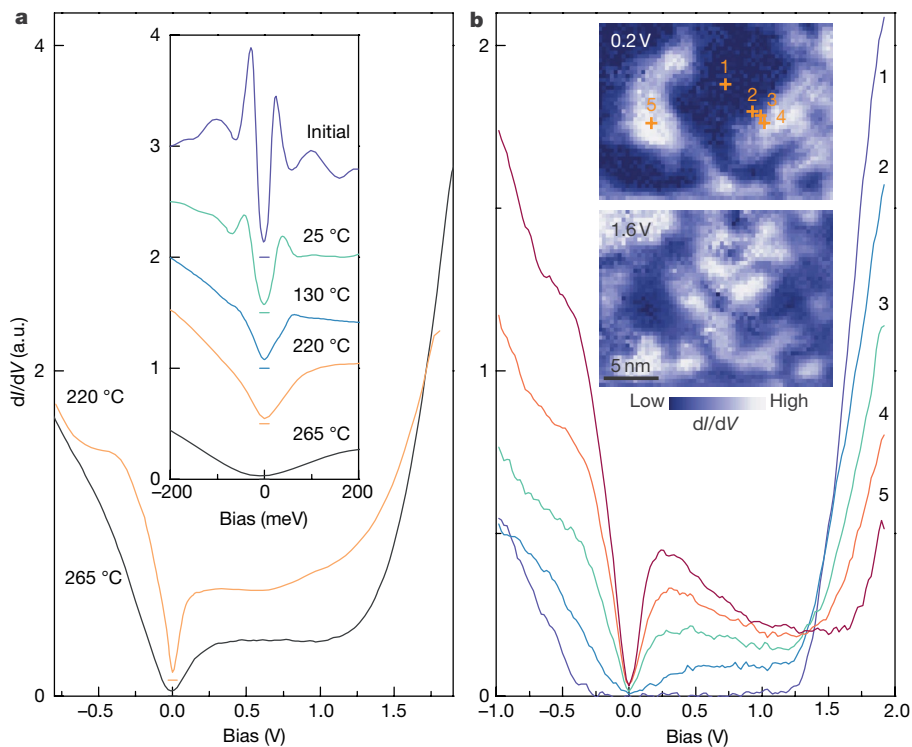


Fig. 6 | Electronic structure of monolayer Bi-2212 in the Mott insulating regime. a, Spatially averaged differential conductance spectra of monolayer Bi-2212 obtained between vacuum annealing cycles. The annealing temperature is marked on each curve. The spectrum labelled ‘Initial’ was recorded before annealing. The as-exfoliated monolayer (obtained from OD55 crystal) was initially over-doped. The annealing cycles progressively lower its doping level

sample to sample. Such deviation is consistent with results from transport measurements; we attribute it to slight loss of oxygen doping (up to 3% in over-doped samples) during sample fabrication. The gap distributions in monolayer and bulk, however, converge if Δ_1 is normalized to $\bar{\Delta}_1$ in each gap map (Fig. 5d). This observation suggests that the microscopic mechanism of the Δ_1 disorder remains the same in the monolayer, even though the monolayer’s dielectric environment is, in absence of the interlayer Coulomb interaction, very different from the bulk.

Despite the large spatial inhomogeneity at high energy scale, a periodic checkerboard charge order emerges outside of the superconducting energy gap in various bulk copper oxides^{12,28,29}. Recent experiments show mounting evidence that a periodic modulation of Cooper pairing—that is, a pair density wave—may coexist with the charge order^{12,31,32}. These charge-ordered states are intimately related to the superconductivity in the CuO_2 plane^{12,29}. An important question is then whether these states persist in the 2D limit. Our conductance mapping of an underdoped monolayer answers the question in the affirmative. As shown in Fig. 5e, a checkerboard pattern is resolved on the conductance map $g(\mathbf{r}, E)$ obtained at $E = 20$ meV. Fourier transform of the map (Fig. 5h) shows that the checkerboard pattern corresponds to wavevector \mathbf{q}_{CO} around $1/4$ of the lattice wavevector $2\pi/a_0$ along the Cu–Cu bond direction (a_0 is the distance between neighbouring Cu atoms). The CO therefore has a real-space wavelength of about $4a_0$, with a correlation length of about $14a_0$ obtained from a Gaussian fit to its peak profile (Extended Data Fig. 10). These results agree well with bulk values^{28,29,34}. As the doping level increases, the CO diminishes and eventually disappears in the over-doped regime (Fig. 5i, j), consistent with observations in bulk copper oxides²⁹. Finally, we present evidence that pair density

and eventually make the specimen extremely under-doped. **b**, Representative tunnelling spectra of the extremely under-doped monolayer in **a**. Inset: tunnelling conductance maps recorded at tunnelling biases of 0.2 V (upper panel) and 1.6 V (lower panel). Crosses mark the positions where the spectra are taken. Spectra are shifted vertically for clarity.

waves also exist in monolayer Bi-2212. Here we examine spatial variation in the amplitude of the coherence peak in the tunnelling spectrum, which empirically correlates with Cooper-pair density modulation in bulk Bi-2212, using the procedure described in ref.³². The coherence peak amplitude map (of the same area as in Fig. 5a, e; Extended Data Fig. 11) exhibits a checkerboard pattern with a period of about $4a_0$ —a clear signature of a pair density wave order.

Electronic structure in the Mott insulating regime

Because oxygen in monolayer Bi-2212 escapes easily at elevated temperatures, we are able to access a wide, continuous doping range in a single specimen by gentle annealing in ultra-high vacuum (Fig. 6a and Extended Data Table 2). Here we focus on the extremely under-doped regime, where the pseudogap and charge-ordered states start to emerge from the parent Mott insulator^{10,34}. Figure 6b displays typical tunnelling spectra obtained on an extremely under-doped monolayer (see inset). The evolution of the spectra is strikingly similar to that in severely under-doped bulk copper oxides^{34,51}. A large charge transfer gap of 1.2 eV is observed on Mott insulating patches. (The gap value is 20% larger than that in bulk Bi-2212 (ref.⁵¹); we attribute the discrepancy to the tip-induced band-bending effect that is common in tunnelling spectroscopy studies of insulators³⁵ and 2D materials⁵².) Outside the Mott insulating patches, a broad in-gap state develops within the charge transfer gap, giving rise to a pseudogap-like spectra around the Fermi level. As in the bulk, the conductance maps at low bias and high bias are anticorrelated (Fig. 6b inset), which implies that the in-gap state comes from spectral weight transfer from the upper Hubbard band of the parent Mott insulator. Our results on monolayers, therefore,

indicate that the dimensionality effect, if it exists at all, does not play an important role in the transition from Mott to pseudogap phase in Bi-2212.

Online content

Any methods, additional references, Nature Research reporting summaries, source data, extended data, supplementary information, acknowledgements, peer review information; details of author contributions and competing interests; and statements of data and code availability are available at <https://doi.org/10.1038/s41586-019-1718-x>.

- Mermin, N. D. & Wagner, H. Absence of ferromagnetism or antiferromagnetism in one- or two-dimensional isotropic Heisenberg models. *Phys. Rev. Lett.* **17**, 1133–1136 (1966).
- Kosterlitz, J. M. & Thouless, D. J. Ordering, metastability and phase transitions in two-dimensional systems. *J. Phys. C* **6**, 1181–1203 (1973).
- Saito, Y., Nojima, T. & Iwasa, Y. Highly crystalline 2D superconductors. *Nat. Rev. Mater.* **2**, 16094 (2017).
- Uchihashi, T. Two-dimensional superconductors with atomic-scale thickness. *Supercond. Sci. Technol.* **30**, 013002 (2017).
- Keimer, B., Kivelson, S. A., Norman, M. R., Uchida, S. & Zaanen, J. From quantum matter to high-temperature superconductivity in copper oxides. *Nature* **518**, 179–186 (2015).
- Chakravarty, S., Sudbo, A., Anderson, P. W. & Strong, S. Interlayer tunneling and gap anisotropy in high-temperature superconductors. *Science* **261**, 337–340 (1993).
- Anderson, P. W. Interlayer tunneling mechanism for high- T_c superconductivity: comparison with c axis infrared experiments. *Science* **268**, 1154–1155 (1995).
- Leggett, A. J. WHERE is the energy saved in cuprate superconductivity? *J. Phys. Chem. Solids* **59**, 1729–1732 (1998).
- Kresin, V. Z. & Moravitz, H. Layer plasmons and high- T_c superconductivity. *Phys. Rev. B* **37**, 7854–7857 (1988).
- Lee, P. A. & Wen, X.-G. Doping a Mott insulator: physics of high-temperature superconductivity. *Rev. Mod. Phys.* **78**, 17–85 (2006).
- Scalapino, D. J. A common thread: the pairing interaction for unconventional superconductors. *Rev. Mod. Phys.* **84**, 1383–1417 (2012).
- Fradkin, E., Kivelson, S. A. & Tranquada, J. M. Colloquium: Theory of intertwined orders in high temperature superconductors. *Rev. Mod. Phys.* **87**, 457–482 (2015).
- Rajasekaran, S. et al. Probing optically silent superfluid stripes in cuprates. *Science* **359**, 575–579 (2018).
- Gerber, S. et al. Three-dimensional charge density wave order in $\text{YBa}_2\text{Cu}_3\text{O}_{6.67}$ at high magnetic fields. *Science* **350**, 949–952 (2015).
- Bluschke, M. et al. Stabilization of three-dimensional charge order in $\text{YBa}_2\text{Cu}_3\text{O}_{6+x}$ via epitaxial growth. *Nat. Commun.* **9**, 2978 (2018).
- Hepting, M. et al. Three-dimensional collective charge excitations in electron-doped copper oxide superconductors. *Nature* **563**, 374 (2018).
- Schneider, T. Dimensional crossover in cuprate superconductors. *Z. Phys. B Condens. Matter* **85**, 187–195 (1991).
- Fischer, Ø., Kugler, M., Maggio-Aprile, I., Berthod, C. & Renner, C. Scanning tunneling spectroscopy of high-temperature superconductors. *Rev. Mod. Phys.* **79**, 353–419 (2007).
- Damascelli, A., Hussain, Z. & Shen, Z.-X. Angle-resolved photoemission studies of the cuprate superconductors. *Rev. Mod. Phys.* **75**, 473–541 (2003).
- Timusk, T. & Statt, B. The pseudogap in high-temperature superconductors: an experimental survey. *Rep. Prog. Phys.* **62**, 61–122 (1999).
- Schmidt, A. R. et al. Electronic structure of the cuprate superconducting and pseudogap phases from spectroscopic imaging STM. *New J. Phys.* **13**, 065014 (2011).
- McElroy, K. et al. Atomic-scale sources and mechanism of nanoscale electronic disorder in $\text{Bi}_2\text{Sr}_2\text{CaCu}_2\text{O}_{8+\delta}$. *Science* **309**, 1048–1052 (2005).
- Kohsaka, Y. et al. How Cooper pairs vanish approaching the Mott insulator in $\text{Bi}_2\text{Sr}_2\text{CaCu}_2\text{O}_{8+\delta}$. *Nature* **454**, 1072–1078 (2008).
- McElroy, K. et al. Relating atomic-scale electronic phenomena to wave-like quasiparticle states in superconducting $\text{Bi}_2\text{Sr}_2\text{CaCu}_2\text{O}_{8+\delta}$. *Nature* **422**, 592–596 (2003).
- Hoffman, J. E. et al. Imaging quasiparticle interference in $\text{Bi}_2\text{Sr}_2\text{CaCu}_2\text{O}_{8+\delta}$. *Science* **297**, 1148–1151 (2002).
- Hanaguri, T. et al. Quasiparticle interference and superconducting gap in $\text{Ca}_{2-x}\text{Na}_x\text{CuO}_2\text{Cl}_2$. *Nat. Phys.* **3**, 865–871 (2007).
- Lang, K. M. et al. Imaging the granular structure of high- T_c superconductivity in underdoped $\text{Bi}_2\text{Sr}_2\text{CaCu}_2\text{O}_{8+\delta}$. *Nature* **415**, 412 (2002).
- Hanaguri, T. et al. A ‘checkerboard’ electronic crystal state in lightly hole-doped $\text{Ca}_{2-x}\text{Na}_x\text{CuO}_2\text{Cl}_2$. *Nature* **430**, 1001–1005 (2004).
- daSilva Neto, E. H. et al. Ubiquitous interplay between charge ordering and high-temperature superconductivity in cuprates. *Science* **343**, 393–396 (2014).
- Comin, R. et al. Charge order driven by Fermi-arc instability in $\text{Bi}_2\text{Sr}_{2-x}\text{La}_x\text{CuO}_{6+\delta}$. *Science* **343**, 390–392 (2014).
- Hamidian, M. H. et al. Detection of a Cooper-pair density wave in $\text{Bi}_2\text{Sr}_2\text{CaCu}_2\text{O}_{8+x}$. *Nature* **532**, 343–347 (2016).
- Ruan, W. et al. Visualization of the periodic modulation of Cooper pairing in a cuprate superconductor. *Nat. Phys.* **14**, 1178 (2018).
- Mesaros, A. et al. Commensurate $4a_0$ -period charge density modulations throughout the $\text{Bi}_2\text{Sr}_2\text{CaCu}_2\text{O}_{8+x}$ pseudogap regime. *Proc. Natl Acad. Sci. USA* **113**, 12661–12666 (2016).
- Cai, P. et al. Visualizing the evolution from the Mott insulator to a charge-ordered insulator in lightly doped cuprates. *Nat. Phys.* **12**, 1047–1051 (2016).
- Kohsaka, Y. et al. Visualization of the emergence of the pseudogap state and the evolution to superconductivity in a lightly hole-doped Mott insulator. *Nat. Phys.* **8**, 534–538 (2012).
- Allredge, J. W. et al. Evolution of the electronic excitation spectrum with strongly diminishing hole density in superconducting $\text{Bi}_2\text{Sr}_2\text{CaCu}_2\text{O}_{8+\delta}$. *Nat. Phys.* **4**, 319–326 (2008).
- Gozar, A. et al. High-temperature interface superconductivity between metallic and insulating copper oxides. *Nature* **455**, 782–785 (2008).
- Bollinger, A. T. & Božović, I. Two-dimensional superconductivity in the cuprates revealed by atomic-layer-by-layer molecular beam epitaxy. *Supercond. Sci. Technol.* **29**, 103001 (2016).
- Terashima, T. et al. Superconductivity of one-unit-cell thick $\text{YBa}_2\text{Cu}_3\text{O}_7$ thin film. *Phys. Rev. Lett.* **67**, 1362–1365 (1991).
- Frindt, R. F. Superconductivity in ultrathin NbSe_2 layers. *Phys. Rev. Lett.* **28**, 299–301 (1972).
- Novoselov, K. S. et al. Two-dimensional atomic crystals. *Proc. Natl Acad. Sci. USA* **102**, 10451–10453 (2005).
- Ajayan, P., Kim, P. & Banerjee, K. Two-dimensional van der Waals materials. *Phys. Today* **69**, 38–44 (2016).
- Sandilands, L. J. et al. Origin of the insulating state in exfoliated high- T_c two-dimensional atomic crystals. *Phys. Rev. B* **90**, 081402(R) (2014).
- Jiang, D. et al. High- T_c superconductivity in ultrathin $\text{Bi}_2\text{Sr}_2\text{CaCu}_2\text{O}_{8+x}$ down to half-unit-cell thickness by protection with graphene. *Nat. Commun.* **5**, 5708 (2014).
- Zaanen, J., Sawatzky, G. A. & Allen, J. W. Band gaps and electronic structure of transition-metal compounds. *Phys. Rev. Lett.* **55**, 418–421 (1985).
- Presland, M. R., Tallon, J. L., Buckley, R. G., Liu, R. S. & Flower, N. E. General trends in oxygen stoichiometry effects on T_c in Bi and Tl superconductors. *Physica C* **176**, 95–105 (1991).
- Huang, Y. et al. Reliable exfoliation of large-area high-quality flakes of graphene and other two-dimensional materials. *ACS Nano* **9**, 10612–10620 (2015).
- Bollinger, A. T. et al. Superconductor–insulator transition in $\text{La}_{2-x}\text{Sr}_x\text{CuO}_4$ at the pair quantum resistance. *Nature* **472**, 458–460 (2011).
- Leng, X., Garcia-Barriocanal, J., Bose, S., Lee, Y. & Goldman, A. M. Electrostatic control of the evolution from a superconducting phase to an insulating phase in ultrathin $\text{YBa}_2\text{Cu}_3\text{O}_{7-x}$ films. *Phys. Rev. Lett.* **107**, 027001 (2011).
- Ando, Y., Komiya, S., Segawa, K., Ono, S. & Kurita, Y. Electronic phase diagram of high- T_c cuprate superconductors from a mapping of the in-plane resistivity curvature. *Phys. Rev. Lett.* **93**, 267001 (2004).
- Ruan, W. et al. Relationship between the parent charge transfer gap and maximum transition temperature in cuprates. *Sci. Bull. (Beijing)* **61**, 1826–1832 (2016).
- Brar, V. W. et al. Gate-controlled ionization and screening of cobalt adatoms on a graphene surface. *Nat. Phys.* **7**, 43–47 (2011).

Publisher's note Springer Nature remains neutral with regard to jurisdictional claims in published maps and institutional affiliations.

© The Author(s), under exclusive licence to Springer Nature Limited 2019

Methods

Fabricating monolayer Bi-2212 for transport measurements

Monolayer flakes of Bi-2212 can be obtained through mechanical exfoliation⁴¹. However, the size of thin flakes tends to be small because brittle Bi-2212 crystals break easily during exfoliation. Activating the SiO₂ surface with oxygen plasma treatment greatly increases the area and yield of monolayer crystals on the SiO₂/Si wafer⁴⁷. We attribute the improvement to the enhanced adhesion between Bi-2212 and SiO₂—the plasma treatment functionalizes the SiO₂ surface with hydroxyl groups that strongly bind to Bi-2212 (ref. ⁵³).

Our systematic investigation (Extended Data Table 1 and Extended Data Fig. 1) reveals that exposing the monolayers to air, albeit briefly, renders them insulating^{41,43,54,55}. An inert Ar atmosphere preserves the superconductivity in the monolayers, but the protection is incomplete: T_c is much suppressed after a prolonged fabrication process at room temperature, and shortening the fabrication time leads to a higher T_c . These observations point to (1) reaction with water vapour in air and (2) rapid oxygen loss at room temperature as two main causes of degradation in monolayer Bi-2212. (The same degradation pathways are also present in bulk crystals^{56–58}.) The oxygen loss, however, slows down considerably at moderately low temperatures, so we are able to obtain high-quality, intrinsic monolayers by fabricating samples on a cold stage kept at -40 °C inside an Ar-filled glove box with water and oxygen content below 0.1 ppm.

To avoid heating during electrode deposition, we make electrical contacts to the exfoliated monolayers by cold-welding indium/gold microelectrodes on the cold stage. Once the device fabrication is complete, we seal each device in a chip carrier (we use ceramic dual-in-line chip carriers) with vacuum grease and a cover glass inside the glove box, and then transfer the whole package into the cryostat. The cover glass comes off once the sample space of the cryostat is evacuated before low-temperature transport measurements, so the doping level can be tuned in situ.

Fabricating monolayer Bi-2212 for STM/STS measurements

We used a vacuum-compatible tape (Kapton tape with silicone adhesive; Accu-Glass Products) to exfoliate thin flakes of Bi-2212 onto Si wafer (covered with a 285-nm-thick SiO₂ layer) in a vacuum chamber with a base pressure of 1×10^{-10} mbar. Few-layer Bi-2212 on the substrate exhibits quantized contrast that correlates well with the number of layers (see also Fig. 1). The correlation makes the search (also done in UHV with $12 \times$ Ultrazoom (Navitar) through a re-entrant viewport) for monolayers convenient. Some of the flakes touch electrodes (Cr/Au with thickness of 2 nm and 3 nm, respectively) in the form of stripes that are patterned on the wafer before the exfoliation; we choose these flakes for STM measurements (Fig. 3a). Except for brief moments when the samples were being transferred to the STM stage, the temperature was always kept below -120 °C. Finally, we confirm the thickness of the samples with AFM outside the UHV after all measurements are completed, to ensure that they were indeed monolayers (Extended Data Fig. 6).

Finite-size scaling analysis of the superconductor-to-insulator transition in monolayer Bi-2212

At the superconductor-to-insulator transition (SIT) in monolayer Bi-2212, HTS emerges from the parent Mott insulator as the sample is doped beyond a critical level. Such a transition is an important example of a continuous quantum phase transition (QPT) that is driven by an external parameter x at absolute zero temperature⁵⁹; the quantum critical point at x_c separates ground states with different symmetry. Exactly how Cooper pairs form in the 2D copper oxide plane and condense into the superconducting phase is a key outstanding question. However, crucial information on the transition can be obtained by investigating the scaling behaviour of $R_{\square}(x, T)$ as x approaches x_c at finite T . This is accomplished by finite-size scaling analysis under the general scheme

of QPT^{60,61}. Near the quantum critical point, the correlation length ξ and correlation time τ become the only characteristic scales in length and time, respectively, and they diverge as $\xi \propto |x - x_c|^{-\nu}$ and $\tau \propto \xi^z \propto |x - x_c|^{-\nu z}$; ν and z are critical exponents. The theory of finite-size scaling asserts that physical quantities have a scaling form that, together with exponents ν and z , depend only on global properties of the system, but not on microscopic details. For 2D SIT, the appropriate finite-size scaling form is⁵⁹:

$$R_{\square}(x, T) = R_c f(|x - x_c| T^{-1/\nu z}). \quad (1)$$

Here the transition is driven by doping variation, so $x \equiv p$; R_c is the critical resistivity at the $p \rightarrow p_c$ and $T \rightarrow 0$ limit, and f is a universal scaling function. Such scaling does not depend on the exact value of p , but the exponent νz and the critical resistivity R_c encode the fundamental properties of the transition. In particular, νz is determined by the universality class that the system belongs to; its value thus provides precious information such as the symmetry of order parameter manifold and types of disorder in 2D Bi-2212 (ref. ⁴⁸).

Extended Data Fig. 4a–c illustrates the finite-size scaling analysis of the SIT in sample A. Following the procedure described in ref. ⁵⁹, we first invert the $R_{\square}(p, T)$ data matrix in Extended Data Fig. 4a, and locate the critical point p_c , where all isotherms converge to $R_{\square} = R_c \approx 10.2$ k Ω (Extended Data Fig. 4b). We then scale the horizontal axis of Extended Data Fig. 4b as $u = |p - p_c| t(T)$ in Extended Data Fig. 4c. Here a single set of temperature-dependent parameters $t(T)$ can force all curves to collapse to a universal scaling function. Further analysis shows that $t(T)$ follows a power law dependence, $t(T) \propto T^{-1/1.53}$ (Extended Data Fig. 5a, blue circles). The SIT in monolayer Bi-2212 is, therefore, well described by continuous 2D QPT, with $\nu z = 1.53$ matching the critical exponents of the SITs driven by ionic gating in thin films of La_{2-x}Sr_xCuO₄ (LSCO, ref. ⁴⁸), lithium-intercalated Bi₂Sr₂CaCu₂O_{8+ δ} (Li₁Bi-2212, ref. ⁶²), and La₂CuO_{4+ δ} (LCO, ref. ⁶³). The close match indicates that the SIT transitions in these copper oxides all belong to the same universality class, even though the critical resistivities differ among these systems.

A survey of critical exponents in copper oxide superconductors, however, shows that not all νz agree with the value in monolayer Bi-2212; various νz values were found to cluster around two different values: 3/2 and 7/3 (refs. ^{48,49,62–64}; Extended Data Fig. 4b, blue squares). It therefore appears that the transitions fall into two distinct universality classes, even though in all copper oxide superconductors the superconductivity arises from doping Mott insulating CuO₂ planes. These observations raise two fundamental questions: (1) what specifically causes the disparate critical exponents in copper oxide superconductors? and (2) what universality classes do they correspond to? We now address these questions by investigating the SIT in monolayer Bi-2212 along another dimension in the parameter space—the disorder level. Here we tune the disorder level by introducing a small amount of air (that contains water vapour, the main degradation agent) into the sample chamber while annealing monolayer Bi-2212 at elevated temperatures.

Extended Data Fig. 4g displays the temperature-dependent resistivity, $R_{\square}(T)$, of a monolayer Bi-2212 (sample C). The sample undergoes a sequence of annealing cycles in 10 mbar of air (containing about 0.3 mbar of water vapour) at room temperature. The curves were obtained between each annealing cycle. We observe that the resistivity drops to zero in two steps as the temperature is lowered. The higher-temperature drop occurs at the apparent T_c of the monolayer, but the resistivity drops to zero only after a second transition at a lower temperature (Extended Data Fig. 4g). Such a two-step transition resembles the superconducting transition in 2D Josephson-coupled superconducting arrays^{65,66} and is ubiquitous in disordered 2D superconducting systems in general^{67,68}. A simplified picture captures the basic physics of the two-step transition: the disordered 2D superconductor can be modelled as superconducting islands embedded in normal metal that provide weak Josephson coupling between the islands. The higher-temperature transition

corresponds to the superconducting transition within the islands, but the entire sample becomes superconducting only when the global, inter-island phase coherence is established after a second transition at a lower temperature⁶⁵.

The SIT takes place at the lower-temperature transition in this disordered monolayer Bi-2212. Because the apparent T_c does not change appreciably during the SIT transition (Extended Data Fig. 4g), the transition is now predominantly driven by disorder that mainly affects the metallic region between the islands. Finally, we perform finite-size scaling analysis of the disorder-driven SIT in monolayer Bi-2212. We parameterize the phenomenological disorder level as $d = \text{const.} / R_{\square}(T = 200 \text{ K})$ (The value of the constant does not affect our analysis; we chose $\text{const.} = 213 \Omega$.) Using the scaling form (1) with $x \equiv d$, we obtained a critical exponent of $\nu z = 2.35$ which is close to $7/3$. The same analysis on a less disordered monolayer yields a similar νz (Extended Data Fig. 4d and Extended Data Fig. 5a).

We can now explain the two disparate critical exponents observed in copper oxide superconductors. We first note that the two distinct critical exponents in monolayer Bi-2212 confirm early observations that SITs in copper oxide superconductors fall into two universality classes. The mystery is, however, resolved—our results show that the two universality classes characterize the doping-driven SIT in the clean limit and the disorder-driven SIT in the dirty limit, respectively. The exponent $\nu z = 7/3$ points towards a quantum percolation model that indeed describes a strongly disordered superconductor⁶⁹. Meanwhile, $\nu z = 3/2$ encodes the essential physics of an intrinsic copper oxide superconductor in both bulk and 2D limits. The fact that bulk and monolayer Bi-2212 belong to the same universality class suggests that the antiferromagnetic order found in bulk Bi-2212 may persist in the monolayer. The microscopic origin of $\nu z = 3/2$ however, remains an open question that requires further investigation.

Data availability

The datasets generated and analysed during the current study are available from the corresponding author on reasonable request.

53. Masteika, V., Kowal, J., Braithwaite, N. S. J. & Rogers, T. A review of hydrophilic silicon wafer bonding. *ECS J. Solid State Sci. Technol.* **3**, Q42–Q54 (2014).
54. Sterpetti, E., Biscaras, J., Erb, A. & Shukla, A. Comprehensive phase diagram of two-dimensional space charge doped $\text{Bi}_2\text{Sr}_2\text{CaCu}_2\text{O}_{8+x}$. *Nat. Commun.* **8**, 2060 (2017).
55. Zhao, S. Y. F. et al. Sign reversing Hall effect in atomically thin high temperature superconductors. *Phys. Rev. Lett.* **122**, 247001 (2019).
56. Jin, S.-G., Zhu, Z.-Z., Liu, L.-M. & Huang, Y.-L. Water reactions of superconducting $\text{Bi}_2\text{Sr}_2\text{CaCu}_2\text{O}_8$ phase at 0 °C and ambient temperature. *Solid State Commun.* **74**, 1087–1090 (1990).
57. Gao, W. & Vander Sande, J. B. The degradation behavior of high- T_c BSCCO/Ag superconducting microcomposites in water. *Mater. Lett.* **12**, 47–53 (1991).
58. Yun, S. H. & Karlsson, U. O. Water degradation of a- and c-axis oriented $\text{HgBa}_2\text{CaCu}_2\text{O}_x$ superconducting thin films. *J. Appl. Phys.* **82**, 6348 (1997).
59. Marković, N., Christiansen, C., Mack, A. M., Huber, W. H. & Goldman, A. M. Superconductor-insulator transition in two dimensions. *Phys. Rev. B* **60**, 4320–4328 (1999).
60. Fisher, M. P. A. Quantum phase transitions in disordered two-dimensional superconductors. *Phys. Rev. Lett.* **65**, 923–926 (1990).

61. Sondhi, S. L., Girvin, S. M., Carini, J. P. & Shahar, D. Continuous quantum phase transitions. *Rev. Mod. Phys.* **69**, 315–333 (1997).
62. Liao, M. et al. Superconductor–insulator transitions in exfoliated $\text{Bi}_2\text{Sr}_2\text{CaCu}_2\text{O}_{8+x}$ flakes. *Nano Lett.* **18**, 5660–5665 (2018).
63. Garcia-Barriocanal, J. et al. Electronically driven superconductor–insulator transition in electrostatically doped $\text{La}_2\text{CuO}_{4+x}$ thin films. *Phys. Rev. B* **87**, 024509 (2013).
64. Zeng, S. W. et al. Two-dimensional superconductor–insulator quantum phase transitions in an electron-doped cuprate. *Phys. Rev. B* **92**, 020503 (2015).
65. Eley, S., Gopalakrishnan, S., Goldbart, P. M. & Mason, N. Approaching zero-temperature metallic states in mesoscopic superconductor–normal–superconductor arrays. *Nat. Phys.* **8**, 59–62 (2012).
66. Böttcher, C. G. L. et al. Superconducting, insulating and anomalous metallic regimes in a gated two-dimensional semiconductor–superconductor array. *Nat. Phys.* **14**, 1138–1144 (2018).
67. Allain, A., Han, Z. & Bouchiat, V. Electrical control of the superconducting-to-insulating transition in graphene–metal hybrids. *Nat. Mater.* **11**, 590–594 (2012).
68. Chen, Z. et al. Carrier density and disorder tuned superconductor-metal transition in a two-dimensional electron system. *Nat. Commun.* **9**, 4008 (2018).
69. Steiner, M. A., Breznay, N. P. & Kapitulnik, A. Approach to a superconductor-to-Bose-insulator transition in disordered films. *Phys. Rev. B* **77**, 212501 (2008).
70. Kim, D. H., Goldman, A. M., Kang, J. H. & Kampwirth, R. T. Kosterlitz–Thouless transition in $\text{Tl}_2\text{Ba}_2\text{CaCu}_2\text{O}_8$ thin films. *Phys. Rev. B* **40**, 8834–8839 (1989).
71. Aslamasov, L. G. & Larkin, A. I. The influence of fluctuation pairing of electrons on the conductivity of normal metal. *Phys. Lett. A* **26**, 238–239 (1968).
72. Ito, T., Takenaka, K. & Uchida, S. Systematic deviation from T -linear behavior in the in-plane resistivity of $\text{YBa}_2\text{Cu}_3\text{O}_{7-y}$: evidence for dominant spin scattering. *Phys. Rev. Lett.* **70**, 3995–3998 (1993).
73. Hüfner, S., Hossain, M. A., Damascelli, A. & Sawatzky, G. A. Two gaps make a high-temperature superconductor? *Rep. Prog. Phys.* **71**, 062501 (2008).

Acknowledgements We thank D.-H. Lee, Z.-Y. Weng, Q.-K. Xue, S.-W. Cheong, Y. Wang, H. Ding and H. Luo for discussions. We also thank X. Jin and D. Feng for their help with the experiment. Part of the sample fabrication was conducted at Nano-fabrication Laboratory at Fudan University. Work at Brookhaven National Laboratory was supported by the Office of Science, US Department of Energy under contract no. DE-SC0012704. Y.Y., L.M. and Y.Z. acknowledge support from the National Key Research Program of China (grant nos. 2016YFA0300703, 2018YFA0305600), National Science Foundation of China (grant nos. U1732274, 11527805, 11425415 and 11421404), Shanghai Municipal Science and Technology Commission (grant no. 18JC1410300) and Strategic Priority Research Program of Chinese Academy of Sciences (grant no. XDB30000000). Y.Y. acknowledges support from the National Postdoctoral Program for Innovative Talents (grant no. BX20180076) and China Postdoctoral Science Foundation (grant no. 2018M641907). P.C. acknowledges support from National Postdoctoral Program for Innovative Talents (grant no. BX201600036), Shanghai Sailing Program (grant no. 17YF1429000), Shanghai Municipal Natural Science Foundation (grant no. 17ZR1442400) and China Postdoctoral Science Foundation (grant no. 2017M610221). X.H.C. acknowledges support from the National Science Foundation of China (grant no. 11888101, 11534010), the National Key R&D Program of China (grant no. 2017YFA0303001 and 2016YFA0300201), Strategic Priority Research Program of the Chinese Academy of Sciences (grant no. XDB25000000) and the Key Research Program of Frontier Sciences, CAS (grant no. QYZDY-SSW-SLH021).

Author contributions The order of the first two authors was determined arbitrarily. Y.Z. conceived the project. Y.Z. and X.H.C. supervised the experiments. R.Z. and G.D.G. synthesized bulk crystals. Y.Y., L.M. and C.Y. developed sample fabrication techniques. Y.Y. did transport measurements. L.M. led the STM study. L.M., P.C. and C.Y. did STM measurements and J.S. provided support. Y.Y., L.M., P.C. and Y.Z. analysed the data and wrote the paper with input from all authors.

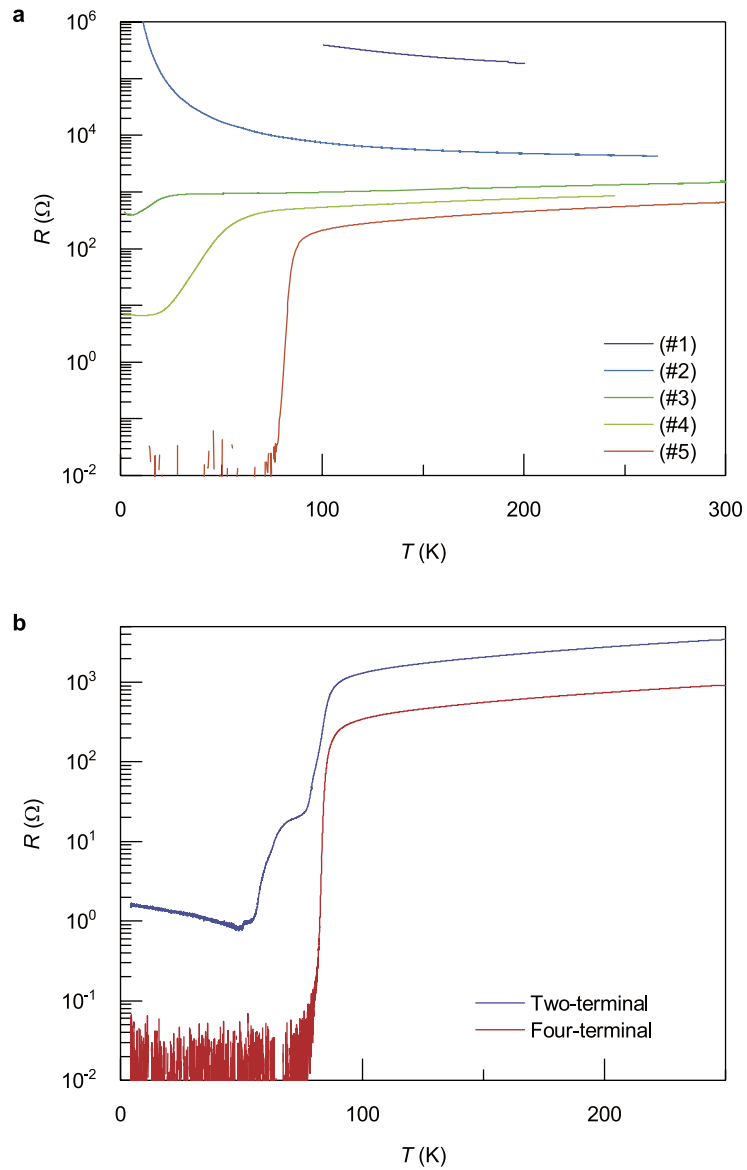
Competing interests The authors declare no competing interests.

Additional information

Correspondence and requests for materials should be addressed to L.M., X.H.C. or Y.Z.

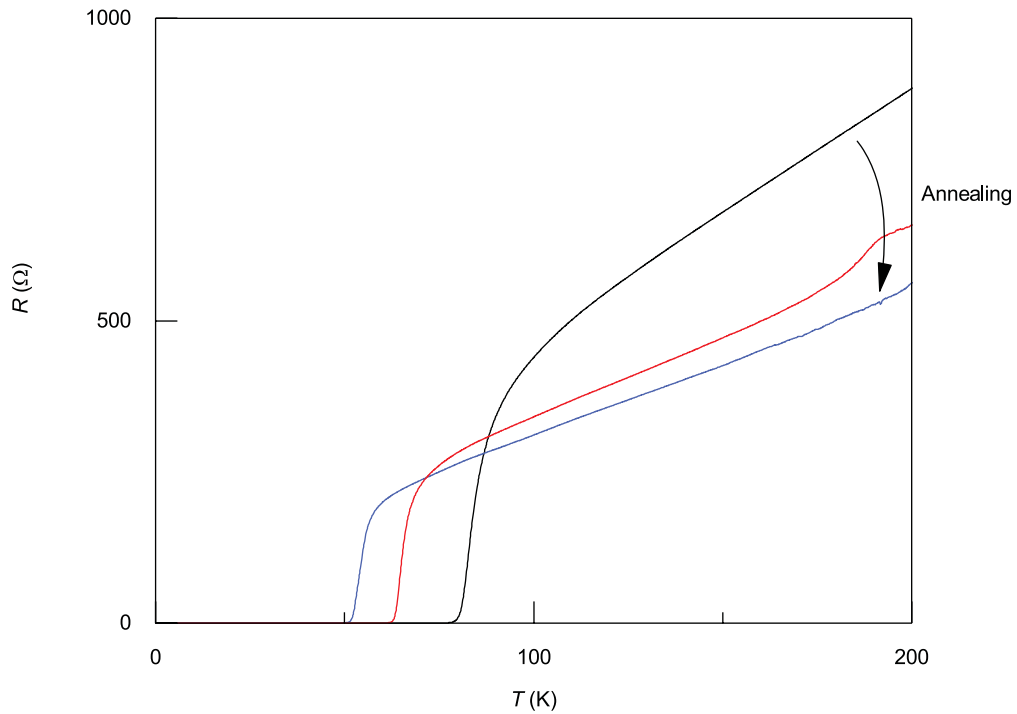
Peer review information Nature thanks Tetsuro Hanaguri and the other, anonymous, reviewer(s) for their contribution to the peer review of this work.

Reprints and permissions information is available at <http://www.nature.com/reprints>.



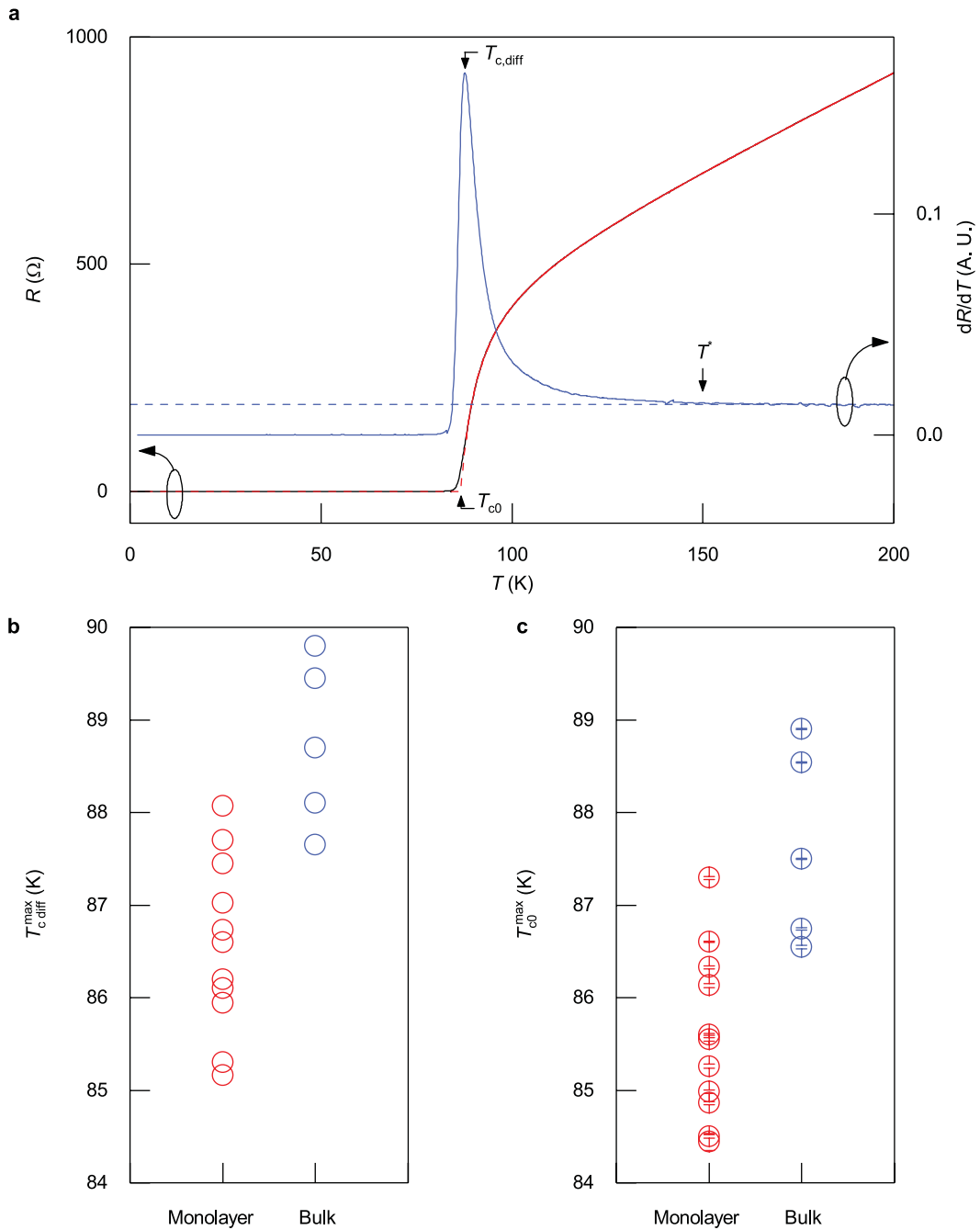
Extended Data Fig. 1 | Transport properties of typical monolayer Bi-2212 samples fabricated by various methods. a, Temperature-dependent resistance of monolayer Bi-2212 samples. Here (#1)–(#5) refer to five typical samples fabricated by different methods indicated in Extended Data Table 1. **b,** Resistance of a typical cold-welded Bi-2212 monolayer device measured with

two-terminal (blue) and four-terminal (red) configurations. The four-terminal configuration is adopted in all our measurements presented in the main text, because it eliminates spurious signals from electrical contacts. The two-terminal resistance in the superconducting state gives an estimate of the contact resistance of the order of 1Ω .



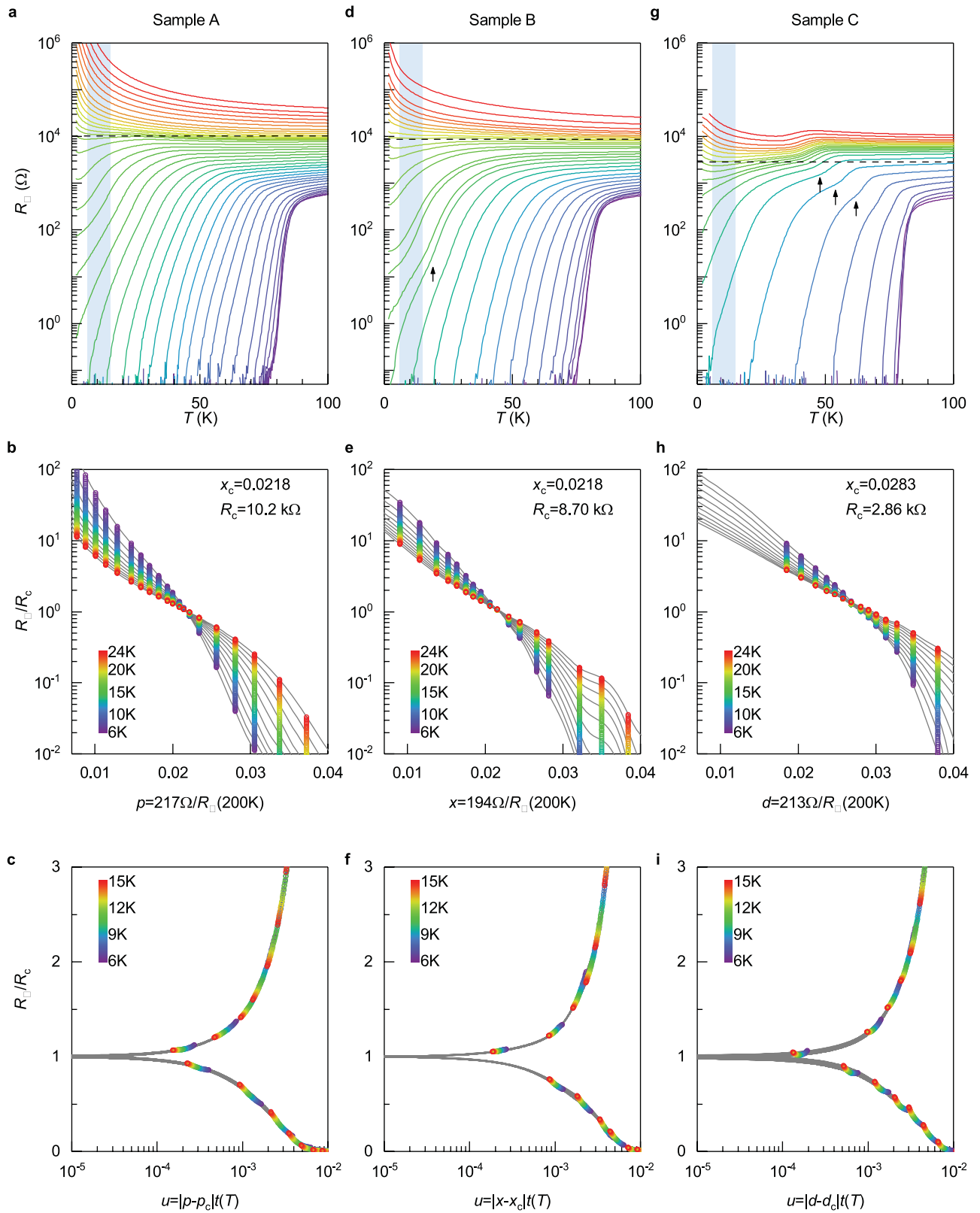
Extended Data Fig. 2 | Temperature-dependent resistance of a monolayer Bi-2212 sample annealed in ozone. Annealing cycles were performed under an O_3 partial pressure of about 50 Pa at temperatures between 220 K and 240 K. O_3 was purged with helium gas between annealing cycles, and data were obtained in helium vapour. Each annealing cycle lasts 5–30 min. Monolayer

Bi-2212 was initially at optimal doping (black curve). The annealing cycles progressively increase the doping level of the sample. The red curve was obtained after first annealing, and blue curve was obtained after second annealing.



Extended Data Fig. 3 | Extracting T_c and T^* from temperature-dependent resistance of monolayer Bi-2212. **a**, Illustration of T_c and T^* extraction from temperature-dependent resistance (black curve, which mostly overlaps with the red curve) and its derivative (blue curve). We used two definitions of T_c in our analysis: (i) $T_{c,diff}$ where the slope of resistance vs temperature curve is maximum⁷⁰; (ii) T_{c0} from fitting with Aslamasov–Larkin paraconductivity model⁷¹ $\Delta\sigma = \sigma(T) - \sigma_{normal}(T) = a(T/T_{c0} - 1)^{-1}$. Near optimal doping, $\sigma_{normal}(T) = (bT + c)^{-1}$, so T_{c0} can be extracted from fitting with

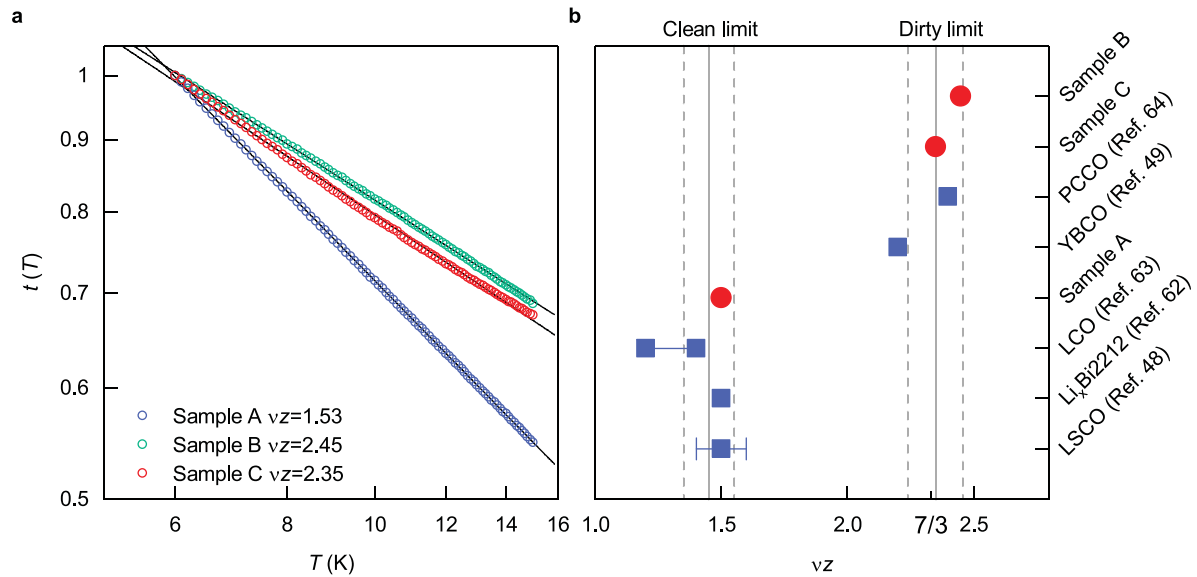
$R(T) = (bT + c)(T - T_{c0}) / (T - T_{c0} + a)$ (red curve). T^* is determined as the temperature at which the derivative of temperature-dependent resistance deviates from constant value (broken blue line; ref. ⁷²). **b**, **c**, $T_{c,diff}^{max}$ (**b**) and T_{c0}^{max} (**c**) of monolayer and bulk Bi-2212. Bulk data were obtained from optimally doped crystals (OP88). Under both definitions, the highest maximum T_c of monolayers is within the statistical uncertainty range of the T_c in optimally doped bulk crystals.



Extended Data Fig. 4 | See next page for caption.

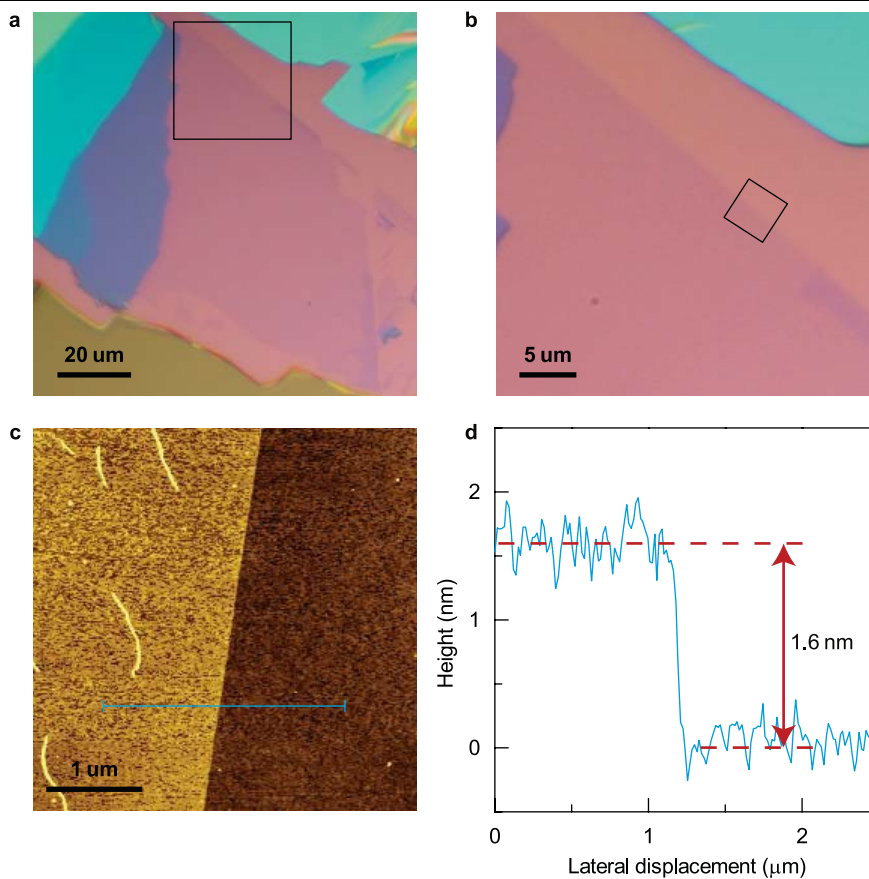
Extended Data Fig. 4 | Superconductor–insulator transition in monolayer Bi-2212. **a**, Temperature-dependent resistivity $R_{\square}(p, T)$ of sample A. The doping level, fixed for each curve, is tuned by repeated annealing cycles under vacuum (pressure below 10^{-4} mbar). The initially superconducting sample becomes insulating via a QPT. Broken line marks the separatrix where the transition occurs. Blue shaded region indicates the temperature range in which we perform the finite-size scaling analysis; the slight up-turn in resistivity at lower temperatures suggests intermediate phase or additional QCP between the superconducting and insulating phases⁴⁹. **b**, Same dataset in **a** plotted inversely, that is, $R_{\square}(p, T)$ plotted as a function of doping level at fixed temperatures between 6 K and 24 K. Each colour refers to a fixed temperature. Continuous curves are interpolations of data points at different temperatures. The point where all curves cross defines the critical point the QPT, ($R_c = 10.2 \pm 0.6$ k Ω , $p_c = 0.022 \pm 0.002$). **c**, Scaling of the same data with respect to variable $u = |p - p_c|t(T)$. A single set of temperature-dependent parameters $t(T)$ can force all data to collapse to a universal scaling function on both sides of the SIT. **d**, Temperature-dependent resistivity of sample B. Data were obtained between annealing cycles performed under 10^{-1} mbar of air that contains about 3×10^{-3} mbar of water vapour. The annealing cycles progressively increase the normal state resistivity, and induces SIT in the monolayer. Blue shaded region marks the temperature range in which we perform the finite-size scaling analysis. **e**, Same resistivity data in **d** plotted as a

function of $x = 194 \Omega/R_{\square}(T = 200$ K). Here x is a phenomenological variable that parametrizes the external factor (doping or disorder level) that drives the SIT; the precise value of x does not affect the finite-size scaling analysis according to formula (1). The critical point of the SIT is identified as ($R_c = 8.7 \pm 0.6$ k Ω , $x_c = 0.022 \pm 0.002$). **f**, Scaling analysis of the dataset in **e**. The analysis yields a critical exponent of $\nu z = 2.45$. The νz differs from the critical exponent in doping-driven SIT in sample A, but coincides with the value in disorder-driven SIT in sample C. Similar to sample C, sample B also features a two-step superconducting transition (marked by black arrow) that indicates considerable amount of disorder. We therefore conclude that disorder level drives the SIT in sample B. **g**, Temperature-dependent resistivity of sample C. Curves are obtained between annealing cycles performed under about 10 mbar of air. Such annealing cycles introduce disorders into the monolayer, and the superconductivity transition occurs in two steps. The disorder-driven SIT takes place at the lower-temperature transition (blue shaded region). **h**, Inverse of the dataset in **g**. Horizontal axis represents the phenomenological disorder level that is parametrized as $d = 213 \Omega/R_{\square}(T = 200$ K). Smooth interpolations of the data points cross at the critical point ($R_c = 2.86 \pm 0.17$ k Ω , $x_c = 0.028 \pm 0.002$). **i**, Scaling of the same data in **h** with respect to variable $u = |d - d_c|t(T)$. $t(T)$ is chosen such that all data collapse to a universal scaling function.



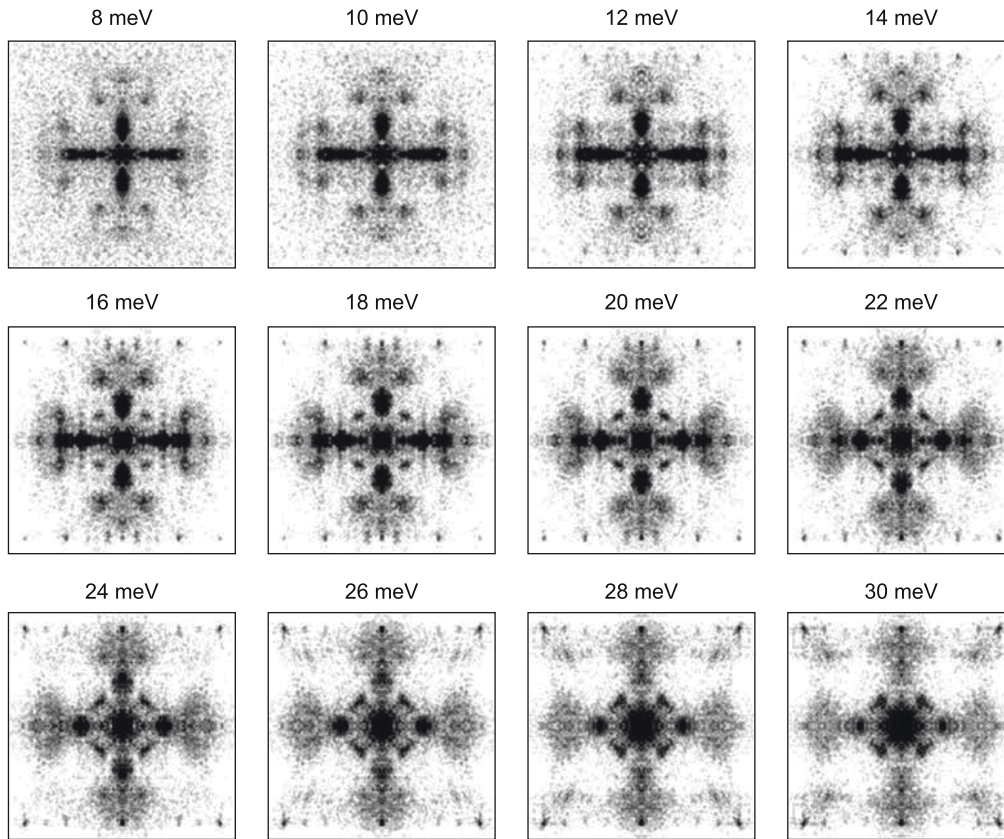
Extended Data Fig. 5 | Critical exponents of superconductor–insulator transitions in copper oxide superconductors. a, Temperature-dependent parameter $t(T)$ obtained from finite-size scaling analysis in Extended Data Fig. 4. Values of $t(T)$ from all three monolayer Bi-2212 samples follow power-law dependence; the slope of the line fits (solid lines) yields the critical exponents of the SIT $\nu_z=1.53, 2.45$ and 2.35 for samples A, B and C, respectively. **b,** Critical

exponents ν_z obtained in monolayer Bi-2212 (red circles) and various other copper oxide superconductors (black squares). All ν_z fall into the neighbourhood of one of the two values, $3/2$ and $7/3$, that characterize the SIT in the clean and dirty limit, respectively (see text). Solid vertical lines mark the mean, and broken lines the standard deviation, of the ν_z values in each category.



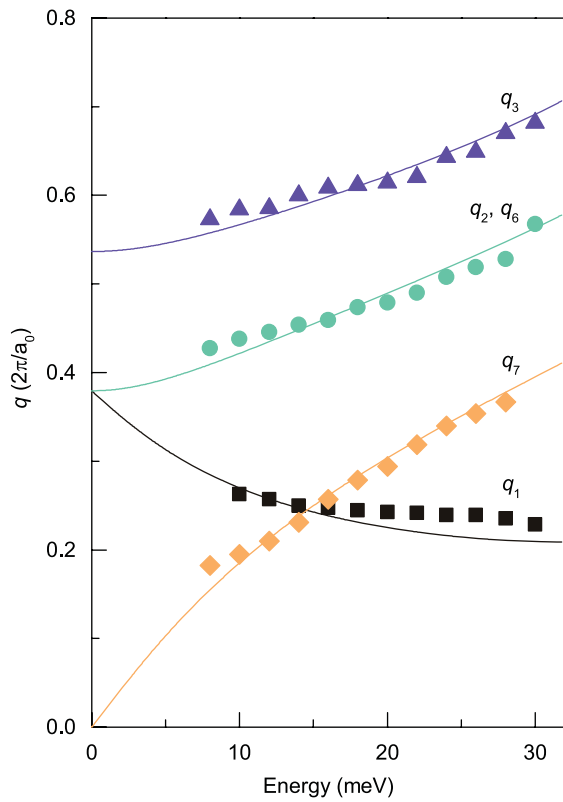
Extended Data Fig. 6 | Characterization of monolayer Bi-2212 after STM measurements. **a**, Optical image of typical Bi-2212 flakes exfoliated on SiO₂/Si substrate. The monolayer (light purple region in the centre) is identified from its optical contrast. **b**, A magnified view of the area marked by the square in **a**. **c**, AFM topography of the area marked by the square in **b**. Both the optical image

and the AFM topography were obtained in an Ar atmosphere inside a glove box after STM measurements performed in UHV. **d**, Line cut of the AFM topography along the line shown in **c**. The step height of about 1.6 nm confirms that the Bi-2212 flake measured in STM was indeed a monolayer.

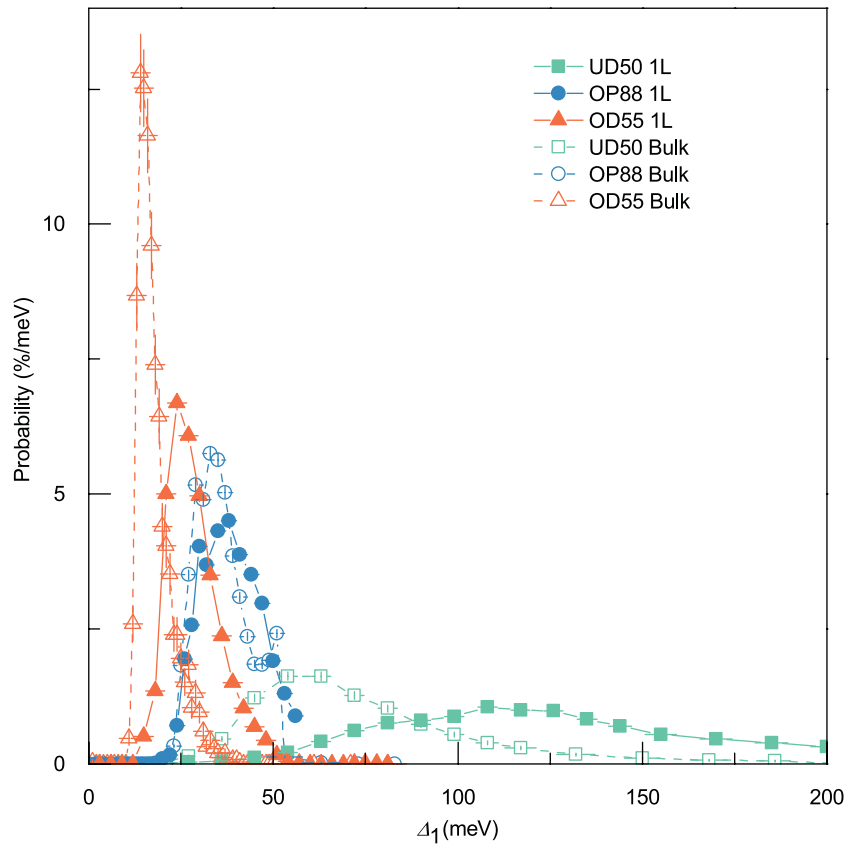


Extended Data Fig. 7 | Fourier transform of the conductance ratio map obtained on monolayer Bi2212 at various energies. Each panel displays a Fourier transform of the conductance ratio map $Z(\mathbf{r}, E)$ of nearly optimally doped monolayer Bi-2212 at the energy labelled on the panel. The $Z(\mathbf{r}, E)$ maps

are obtained from a set of 200×200 -pixel conductance maps taken on an area of $500 \text{ \AA} \times 500 \text{ \AA}$ with an energy resolution of 2 meV. Data were obtained from the same sample in Fig. 4 (here we show the full dataset).

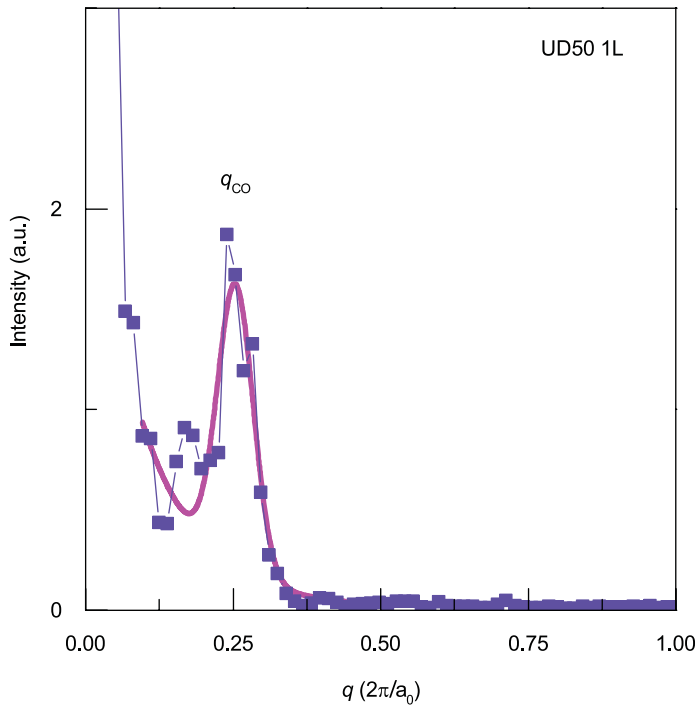


Extended Data Fig. 8 | Energy dispersion of the q-vectors. Amplitudes of measured q_i (in units of $2\pi/a_0$) are plotted as functions of energy ($i=1 \dots 7$, except that q_4 and q_5 are too weak to be detected). We followed the method described in ref.²³ to obtain q_1 . Solid lines are energy dispersion of the q-vectors expected in the octet model.

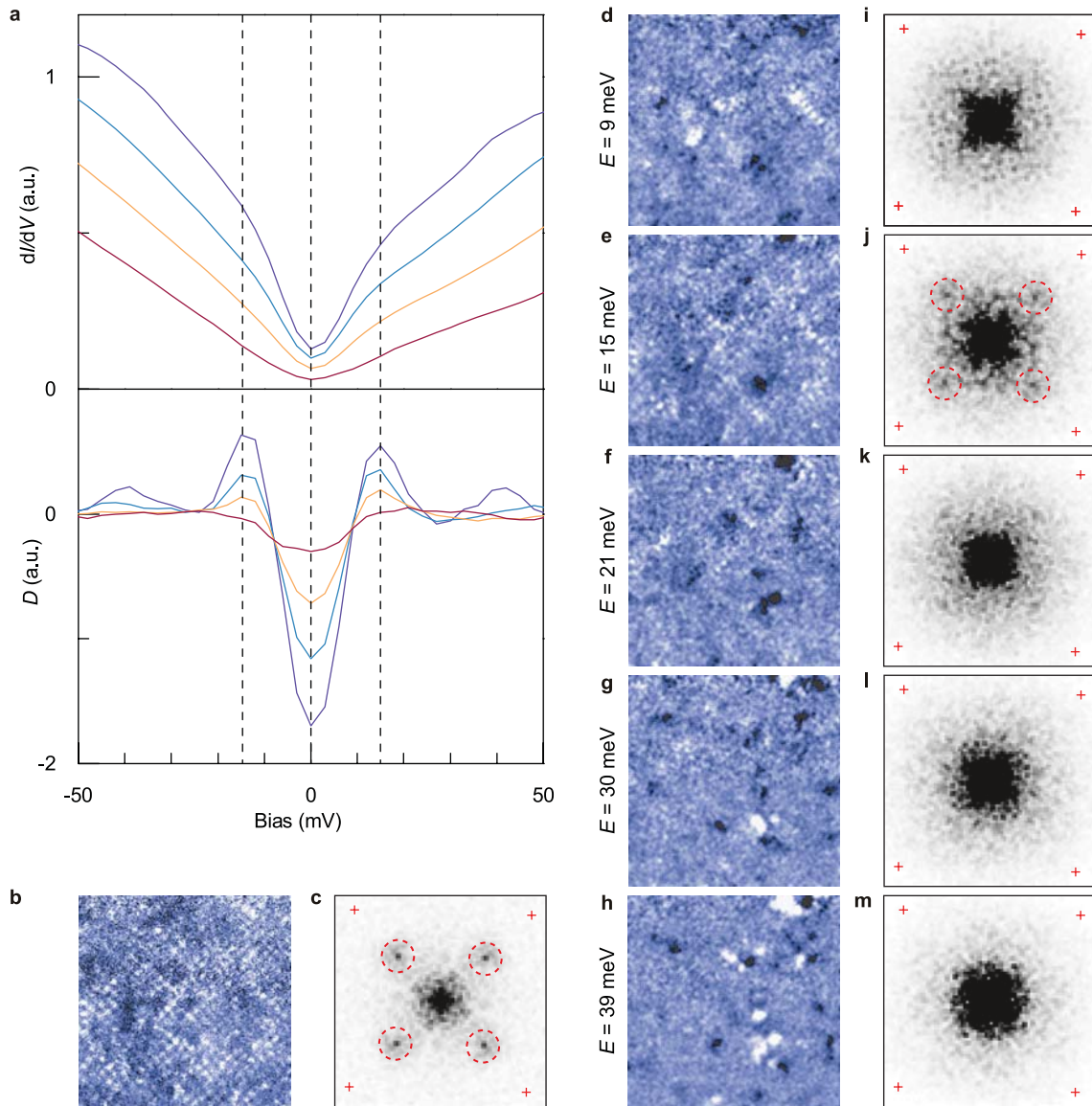


Extended Data Fig. 9 | Histograms of $\Delta_1(r)$ gap maps in monolayer and bulk Bi-2212. Solid and empty symbols represent data from monolayer and bulk Bi-2212, respectively. Δ_1 distributions in monolayers shift towards higher energies compared with those in bulk crystals. The shift reflects slight loss of oxygen doping during monolayer sample fabrication. Specifically, the doping level p is directly related to the average value of the pseudogap. From the average pseudogap, we estimate that $p = 0.06 \pm 0.02$, 0.16 ± 0.02 and 0.19 ± 0.02 for

monolayers obtained from UD50, OP88 and OD55, respectively^{23,36,73}. These values are lower than the doping levels extracted in the bulk crystals ($p = 0.08 \pm 0.02$, 0.17 ± 0.02 and 0.22 ± 0.01 for UD50, OP88 and OD55, respectively). Here we used the relations $2\Delta_1 = 152 \text{ meV} \times (0.27 - p)/0.22$ for $0.1 < p < 0.22$ and $2\Delta_1 = 85 \text{ meV} \times (0.12 - p)/0.02$ for $0.06 < p < 0.08$ to estimate the doping level in both bulk crystals and monolayers.



Extended Data Fig. 10 | Wavevector of the CDW order in monolayer Bi-2212 obtained in UD50. Line cut (blue line) of the FFT of $g(\mathbf{r}, E = 20 \text{ meV})$ map in Fig. 5h along the Cu–O bond direction exhibits a peak at $q_{CO} = 0.25 (2\pi/a_0)$ that is associated with the charge-ordered state. The magenta line is a Gaussian fit to the peak plus a decaying exponential background. The full-width at half-maximum of the peak yields a correlation length of about $14a_0$.



Extended Data Fig. 11 | Pair density wave in monolayer Bi-2212. **a**, Four representative conductance spectra (dI/dV ; upper panel) and the negative of their second derivative ($D = -d^3I/dV^3$; lower panel) in under-doped monolayer Bi-2212 obtained from UDSO. We additionally define $H = dI/dV(E = \Delta_0) - dI/dV(E = 0)$, which corresponds to the amount of low-energy DOS gapped out by Cooper pairing (here $\Delta_0 = 15$ meV). The pair density wave can be visualized by spatially mapping either H or D (ref. ³²). **b**, $H(\mathbf{r})$ map on a $40 \text{ nm} \times 40 \text{ nm}$ area. A checkerboard pattern is clearly resolved. **c**, Fourier transform of the $H(\mathbf{r})$ map in **b**. Peaks at $|\mathbf{q}| = (0.25 \pm 0.02)2\pi/a_0$ (marked by broken circles) along the Cu-O bond directions indicate the emergence of pair density wave order³². **d-h**, $D(\mathbf{r})$ maps obtained on the same area in **b** at various energies. **i-m**, Fourier transform

of the $D(\mathbf{r})$ maps in **d-h**. The $|\mathbf{q}| = 2\pi/4a_0$ spatial modulations at $E = 15$ meV (broken circles in **j**) again indicate the existence of pair density wave³². Red crosses mark $\mathbf{q} = (0, \pm\pi/a_0)$ and $(\pm\pi/a_0, 0)$. We followed the method described in ref. ³² to obtain $H(\mathbf{r})$ and $D(\mathbf{r})$ maps. First, a set of conductance (dI/dV) spectra was taken on a 160×160 grid over the $40 \text{ nm} \times 40 \text{ nm}$ area. Here we used a set-point bias voltage of -300 mV, which is far beyond the energy scale of the charge-ordered state, to eliminate possible set-point effects. We then fitted each dI/dV spectrum with a second-order polynomial, and took the second derivative of the polynomial to obtain the D spectrum. The $H(\mathbf{r})$ map is directly obtained from the dI/dV spectra grid.

Extended Data Table 1 | Optimizing fabrication process for monolayer and bilayer Bi-2212 samples

	Contact method	Air-exposure time	Total fabrication time in glove box	Bulk crystal	# of devices	T_c
Bilayer	Metal evaporation at room temperature	5 min	4 h	OP88	5	50 - 70 K
	Pre-patterned bottom contact	2 s	2 h	OP88	1	~ 70 K
	Pre-patterned bottom contact	2 s	2 h	OD55	1	80 - 90 K
	Cold welding	/	2 h	OP88	4	80 - 90 K
Monolayer	Metal evaporation at room temperature	5 min	4 h	OP88	2	Insulating
	Prepatterned bottom contact ^(#1)	2 s	2 h	OP88	3	Insulating
	Pre-patterned bottom contact	2 s	2 h	OD55	1	Insulating
	Metal evaporation at room temperature ^(#2)	/	4h	OP88	2	Insulating
	Metal evaporation at low temperature (~ 100 K) ^(#3)	/	4 h	OD55	3	< 10 K
	Cold welding ^(#4)	/	2 h	OP88	2	< 40 K
	Cold welding	/	2 h	OD55	4	70 - 80 K
	Cold welding ^(#5)	/	0.5 - 1 h	OD55	14	80 - 90 K

We have systematically investigated the effects of the following key factors on the transport properties of monolayer and bilayer Bi-2212: contact method, air-exposure time and total fabrication time in glove box. We observe that monolayer Bi-2212 is more prone to degradation than is bilayer graphene. In particular, exposure to air is most detrimental to sample quality of the monolayers. Evaporating metal contacts (through shadow mask) also causes considerable degradation. We find that cold-welding indium contacts in the glove box preserves the monolayer sample quality. Here, thin indium foils make stable contacts with a thick flake that is connected to the monolayer, so that the thick flake electrically bridges the indium electrodes and the monolayer (Fig. 1e). The monolayer samples exfoliated from an over-doped crystal (OD55) are slightly over-doped, and their maximum T_c is comparable to the T_c of optimally doped bulk crystals (Fig. 2c).

^{(#1)-(#5)}Transport properties of typical monolayer samples from these categories are shown in Extended Data Fig. 1.

Extended Data Table 2 | Annealing sequence of monolayer Bi-2212

Annealing temperature	Annealing time	Doping regime	Δ_1 (meV)
As-exfoliated	/	Over-doped	28 ± 1
25 °C	1 week	Nearly optimally doped	40 ± 1
130 °C	30 min	Under-doped	56 ± 1
220 °C	30 min	Under-doped	122 ± 4
265 °C	30 min	Extremely under-doped	250 ± 20

This sequence relates to the monolayer Bi-2212 shown in Fig. 6. The as-exfoliated monolayer Bi-2212 (over-doped; $\Delta_1 = 28 \pm 1$ meV) was annealed under UHV with a base pressure of 1×10^{-10} mbar. The pseudogaps Δ_1 were extracted from spatially averaged conductance spectra.